
Evolution and Statistics of Non-Sphericity of Dark Matter Halos from Cosmological N-Body Simulation

Daichi Suto ¹, Tetsu Kitayama ², Takahiro Nishimichi ^{3,4}, Shin Sasaki ⁵,
Yasushi Suto ^{1,6}

¹Department of Physics, The University of Tokyo, Tokyo 113-0033, Japan

²Department of Physics, Toho University, Funabashi, Chiba 274-8510, Japan

³Kavli Institute for the Physics and Mathematics of the Universe (WPI), The University of Tokyo Institutes for Advanced Study, The University of Tokyo, 5-1-5 Kashiwanoha, Kashiwa 277-8583, Japan

⁴CREST, JST, 4-1-8 Honcho, Kawaguchi, Saitama, 332-0012, Japan

⁵Department of Physics, Tokyo Metropolitan University, Hachioji, Tokyo 192-0397, Japan

⁶Research Center for the Early Universe, School of Science, The University of Tokyo, Tokyo 113-0033, Japan

*E-mail: daichi@utap.phys.s.u-tokyo.ac.jp

Received ; Accepted

Abstract

We revisit the non-sphericity of cluster-mass scale halos from cosmological N-body simulation on the basis of triaxial modelling. In order to understand the difference between the simulation results and the conventional ellipsoidal collapse model (EC), we first consider the evolution of *individual* simulated halos. The major difference between EC and the simulation becomes appreciable after the turn-around epoch. Moreover, it is sensitive to the individual evolution history of each halo. Despite such strong dependence on individual halos, the resulting non-sphericity of halos exhibits weak but robust mass dependence in a *statistical* fashion; massive halos are more spherical up to the turn-around, but gradually become less spherical by $z = 0$. This is clearly inconsistent with the EC prediction; massive halos are usually more spherical. In

addition, at $z=0$, inner regions of the simulated halos are less spherical than outer regions, i.e., the density distribution inside the halos is highly inhomogeneous and therefore not self-similar (concentric ellipsoids with the same axis ratio and orientation). This is also inconsistent with the homogeneous density distribution that is commonly assumed in EC. Since most of previous fitting formulae for the probability distribution function (PDF) of axis ratio of triaxial ellipsoids have been constructed under the self-similarity assumption, they are not accurate. Indeed, we compute the PDF of *projected* axis ratio a_1/a_2 directly from the simulation data *without* the self-similarity assumption, and find that it is very sensitive to the assumption. The latter needs to be carefully taken into account in direct comparison with observations, and therefore we provide an empirical fitting formula for the PDF of a_1/a_2 . Our preliminary analysis suggests that the derived PDF of a_1/a_2 roughly agrees with the current weak-lensing observations. More importantly, the present results will be useful in future exploration of the non-sphericity of clusters in X-ray and optical observations.

Key words: Cosmology: dark matter; large-scale structure of Universe; Galaxies: clusters: general

1 Introduction

Dark matter halos serve as building blocks in the structure formation in the universe. While the spherical assumption for shapes of dark matter halos has been widely used both in theoretical and observational researches, a number of observations and cosmological simulations has exhibited clear signatures of the non-sphericity of dark matter halos.

It is conventionally accepted that the primordial density fluctuations in the early universe obey the Gaussian random field, and they have a definite statistical signature of the non-sphericity (Doroshkevich 1970; Bardeen et al. 1986). One prescription for the non-spherical evolution of such primordial density fluctuations is given by the ellipsoidal collapse model (hereafter EC; White & Silk 1979; Bond & Myers 1996). By taking account of the non-spherical evolution of halos, Sheth & Tormen (2002) found that the mass function fits better the simulation results than that of spherical prediction based on the Press-Schechter theory (Press & Schechter 1974).

The improved quality of observational data demands more accurate theoretical models of the non-sphericity of halos beyond the simple EC prediction. However, purely theoretical description of the non-spherical structure and evolution of dark matter halos is very difficult due to the non-linear evolution and complicated interactions among dark matter within the highly inhomogeneous density

distribution. Therefore cosmological N-body simulations play key roles in investigating the non-sphericity of halos. In fact, many authors have recently studied the non-sphericity of halos extracted from cosmological N-body simulations (Jing & Suto 2002; Ludlow & Porciani 2011; Schneider et al. 2012; Bryan et al. 2013; Despali et al. 2013, 2014; Borzyszkowski et al. 2014; Ludlow et al. 2014; Butsky et al. 2015; Velliscig et al. 2015; Bonamigo et al. 2015; Vega et al. 2016).

In particular, Jing & Suto (2002) (hereafter JS02) modelled simulated halos by triaxial ellipsoids, and found that their minor-to-major axis ratio follows a universal probability distribution function (PDF) that depends on redshift and mass. Rossi et al. (2011) found that the PDF of JS02 contradicts the prediction of EC with the Gaussian random initial conditions; while massive halos are more spherical in EC, they are less spherical in JS02. Bonamigo et al. (2015) and Vega et al. (2016) performed improved N-body simulations for halos with higher resolution in a wider mass range, and they confirmed that their results basically reproduce JS02, still in disagreement with EC.

Even from the existing observation data, the non-sphericity of halos is already detectable especially for galaxy clusters in X-ray and optical bands. Since observational analyses are based on the density distribution of halos *projected on the sky*, the projected (two-dimensional) non-sphericity is more relevant quantity than the three-dimensional one. In fact, Oguri et al. (2003) (hereafter OLS03) calculated the PDF of projected axis ratio by integrating the PDF of JS02. Then they showed that the observed excess of gravitationally lensed arcs relative to the spherical model prediction can be reconciled by taking into account the effect of the non-sphericity of lensing halos. The PDF of the non-sphericity has been also observationally examined, although the observational uncertainty is large at this stage. The weak lensing study by Oguri et al. (2010) showed that their 18 clusters have a PDF of ellipticity barely consistent with that proposed by JS02. The 70 X-ray clusters analyzed by Kawahara (2010) with the hydrostatic equilibrium assumption also produced a roughly consistent result with JS02. At this stage, the available data is limited and the observational uncertainty is large. In the near future, however, especially Subaru Hyper Suprime-Cam¹ will provide us with a number of highly resolved lensing halos that are suitable for non-spherical analyses.

We emphasize that the PDF of JS02, and therefore that of OLS03 assume the self-similarity of the halo structure; the density distribution of halos is approximated by concentric ellipsoids with the same axis ratio and orientation. As JS02 have already indicated, however, the simulated halos are not necessarily self-similar. In order to fully utilize the data by future observations, an improved model of the projected axis ratio is quite important.

Therefore, our goal in this paper is to find an empirical fitting formula for the PDF of projected axis ratio of dark matter halos without assuming their self-similarity. For that purpose, we analyze

¹ www.naoj.org/Projects/HSC/

2004 halos extracted from N-body simulation, and approximate the density distribution around each simulated halo and its protohalos by triaxial ellipsoids. To better understand the non-spherical evolution of the halos, we first compare the evolution of individual halos with the EC prediction. Next we statistically examine the mass dependence and the radial profile of axis ratio of the simulated halos, and identify how and when the difference between EC and simulations emerges. Importantly, we find that the self-similarity assumption for halos adopted in the previous studies (JS02; OLS03) is not accurate, and that the prediction of the projected non-sphericity of dark matter halos is significantly affected by the assumption. Therefore we calculate the PDF of the projected axis ratio directly from the simulation data. This is exactly what we aim at in this paper.

The rest of this paper is organized as follows. Section 2 describes our N-body simulation and how to follow the evolution of our simulated halos. We compare the evolution of individual halos with EC in Section 3. Section 4 discusses the statistical evolution of halo non-sphericity. In Section 5, we present the PDF of axis ratio of halos in three-dimensional space, and its two-dimensional counterparts are constructed. Finally Section 6 summarizes this paper.

2 Triaxial Modelling of Simulated Halos

2.1 N-body simulation

Throughout this paper, we use cluster-scale halos identified from a cosmological N-body simulation. The details of the simulation and the halo-finding procedures are described in this subsection.

We start the simulation at $z = 99$, where $N = 1024^3$ particles distributed in a periodic cube with a side length of $360 h^{-1}\text{Mpc}$ (comoving). Their initial conditions are generated with a parallel code developed by Nishimichi et al. (2009) and Valageas & Nishimichi (2011), which is based on the second-order Lagrangian perturbation theory (Scoccimarro 1998; Crocce, Pueblas & Scoccimarro 2006).

We employ the matter transfer function computed by a linear Boltzmann solver CAMB (Lewis et al. 2000) for a flat ΛCDM cosmology with the nine-year WMAP parameters (Hinshaw et al. 2013); $\Omega_{\text{m},0} = 0.279$, $h = 0.7$, $n_{\text{s}} = 0.972$, and $\sigma_8 = 0.821$ are the current matter density in units of the critical density, the Hubble constant in units of $100 \text{ km s}^{-1} \text{ Mpc}^{-1}$, the scalar spectral index, and the amplitude of the density fluctuation (linearly extrapolated to the present) smoothed with a top-hat filter of radius $8 h^{-1}\text{Mpc}$, respectively. With the above parameters, mass of each simulation particle m_{particle} is $3.4 \times 10^9 h^{-1} M_{\odot}$, which is sufficient to resolve massive halos ($\gtrsim 10^{14} h^{-1} M_{\odot}$) at $z = 0$.

The particle distribution is then evolved using a publicly available parallel cosmological N-body solver Gadget2 (Springel 2005). The long-range gravitational force is computed on 2048^3 mesh

points based on the fast Fourier transform, while we rely on the tree algorithm with the softening length of $20 h^{-1} \text{kpc}$ on short range. We store snapshots at redshifts $z = 49, 9, 5, 4, 3, 2, 1.5, 1, 0.8, 0.6, 0.4, 0.2, 0.1$ and 0 . Halos at $z = 0$ are identified using the friends-of-friends (FOF) algorithm (Davis et al. 1985) with the linking length of 0.159 times the mean inter-particle separation in one dimension. This length is chosen so that the corresponding virial overdensity Δ_{vir} matches 355.4 in units of the cosmic mean density at $z = 0$, which is motivated by the spherical collapse model (Gunn & Gott 1972; Gunn 1977; Peebles 1980). Indeed, we confirmed that the total mass of the linked particles M_{FOF} approximately corresponds to the virial mass M_{vir} . We further apply the SUBFIND algorithm (Springel et al. 2001) implemented in Nishimichi & Oka (2014) for each FOF halo to identify substructures as well as unbound particles.

In this paper, we use the FOF halos with $M_{\text{FOF}} > 6.25 \times 10^{13} h^{-1} M_{\odot}$, corresponding to the mass range of galaxy clusters which are well resolved in optical and X-ray observations. The total number of those halos is 2004.

2.2 Morphology of FOF halos

Before modelling the 2004 simulated halos by triaxial ellipsoids, we classify the halos by the amount of substructures. This is useful in understanding the extent to which the definition of the non-sphericity of the FOF halos is sensitive to the presence of substructures.

Due to the nature of the FOF algorithm, an FOF halo may comprise two or more prominent components. Such a halo tends to yield higher non-sphericity, which should be distinguished from a very elongated *single* structure.

According to the result of the SUBFIND algorithm, we obtain the mass M_i of the i -th most massive component for each FOF halo. The most massive component ($i = 1$) is called the “main halo”, and we call the other components “substructures”. Since the shape of a cluster is expected to be sensitive to a few prominent substructures, we classify halos according to the values of M_2/M_1 and M_3/M_1 , instead of the total mass fraction of substructures. We note that this classification is free from numerical resolutions because such big substructures are all well-resolved in the current simulation.

The upper-left, upper-right and lower-left panels of Figure 1 show the snapshots of FOF member particles of three halos with different morphology. The halo in the upper-left panel has very small values of M_2/M_1 and M_3/M_1 , representing a single isolated structure. In contrast, the halo in the upper-right panel has relatively large M_2/M_1 and small M_3/M_1 , corresponding to a “double-structure”. The third halo in the lower-left panel has relatively large values both for M_2/M_1 and

| $M/10^{14}h^{-1}M_{\odot}$ | | > 2.5 | 1.25 - 2.5 | 0.625 - 1.25 | total |
|----------------------------|-----------------|-------|------------|--------------|-------|
| single | $M_2/M_1 < 0.2$ | 171 | 429 | 1172 | 1772 |
| multiple | $M_2/M_1 > 0.2$ | 32 | 68 | 132 | 232 |
| total | | 203 | 497 | 1304 | 2004 |

Table 1. The numbers of single- and multiple-halos, where M_1 and M_2 are the masses of the main halo and the most massive substructure.

M_3/M_1 , and is classified as a “triple-structure”.

The lower-right panel of Figure 1 indicates the cumulative fraction of the halos with a given threshold of M_2/M_1 or M_3/M_1 . The majority of our halos have small M_2/M_1 , and M_3 is substantially smaller than M_2 . Thus the multiplicity of most of the halos can be characterized by the value of M_2/M_1 . For later convenience, we set the threshold of $M_2/M_1 = 0.2$, and call a halo with $M_2/M_1 < 0.2$ a “single-halo”. Also, a halo with $M_2/M_1 > 0.2$ is referred to as a “multiple-halo”. Then the halos in the upper-right and the lower-left panels of Figure 1 are multiple-halos. Such multiple-halos occupy approximately 10 % of all the 2004 halos.

The threshold $M_2/M_1 = 0.2$ is somewhat arbitrary. According to the right panel of Figure 1, if we set the threshold by $M_2/M_1 = 0.1$, for example, ~ 20 % of our sample are classified as multiple-halos. As will be seen in the later sections, the choice of the threshold does not make a major difference in the main results of this paper.

Table 1 lists the number of the single- and multiple-halos out of our sample, corresponding to the threshold $M_2/M_1 = 0.2$.

2.3 Comparison of different methods of triaxial modelling: mass tensor vs. isodensity surface

Throughout this paper, we approximate the density distribution of the simulated halos by a triaxial ellipsoid with the axis lengths A_k ($k = 1, 2, 3$). The boundary of the ellipsoid is described by

$$\left(\frac{x_1}{A_1}\right)^2 + \left(\frac{x_2}{A_2}\right)^2 + \left(\frac{x_3}{A_3}\right)^2 = 1, \quad (1)$$

where x_k ($k = 1, 2, 3$) denotes the coordinate defined along the three axes with the origin set to the center of the ellipsoid.

One measure of the non-sphericity of each halo is the minor-to-major axis ratio A_1/A_3 . The ellipticity e :

$$e = \frac{A_3 - A_1}{2(A_1 + A_2 + A_3)}. \quad (2)$$

is also used as an indicator of the non-sphericity in the literature. Thus we consider both A_1/A_3 and e

in the following sections. For example, a sphere has $e = 0$ and $A_1/A_3 = 1$. Also, for an ellipsoid with $A_1/A_3 = 0.5$, $0.1 \leq e \leq 0.125$, depending on A_2 ; e is primarily determined by the deference between A_1 and A_3 , whereas it also depends on A_2 (or prolateness).

The values of axis lengths A_k are not constant for an entire simulated halo. Within the approximation of triaxial modelling, A_k should be expressed as $A_k(M_{\text{ellipsoid}})$, where $M_{\text{ellipsoid}}$ is the mass enclosed by the ellipsoid. Accordingly, A_1/A_3 and e also depend on $M_{\text{ellipsoid}}$.

In this paper, we compute the axis lengths $A_k(M_{\text{ellipsoid}})$ on the basis of the mass tensor $I_{\alpha\beta}$ (defined below) in an iterative fashion as follows. For a given set of $A_k(M_{\text{ellipsoid}})$, we compute the mass tensor $I_{\alpha\beta}$:

$$I_{\alpha\beta} = \sum_{i=1}^N x_{\alpha}^{(i)} x_{\beta}^{(i)}, \quad (3)$$

where $x_{\alpha}^{(i)}$ ($\alpha = 1, 2, 3$) is the coordinate of the i -th particle along the three axes of the ellipsoid, and the summation is taken over the $N(= M_{\text{ellipsoid}}/m_{\text{particle}})$ particles inside the ellipsoid. That mass tensor is now diagonalized and rotate the coordinate accordingly. The square root of the eigenvalues multiplied by some constant now become a new set of axis lengths $A_k(M_{\text{ellipsoid}})$. The constant is determined so that the ellipsoid encloses $M_{\text{ellipsoid}}$. The coordinate system is redefined along the new axis lengths $A_k(M_{\text{ellipsoid}})$, and the center is reset to the center-of-mass of the particles inside the new ellipsoid. Starting from the sphere centered on the center-of-mass of the FOF members, the above procedure is iterated until all the eigenvalues converge within one percent. In the above procedure, we use the all the particles *including substructures and non-FOF members*.

In literature, there are several methods to determine the axis lengths A_k of simulated halos, including isodensity surfaces and other definitions of mass tensors (JS02; Despali et al. 2014; Ludlow et al. 2014; Bonamigo et al. 2015; Vega et al. 2016). We decide to adopt the definition (3), and we explain why we prefer this estimator of the non-sphericity in what follows.

An alternative method to determine A_k is the direct fitting to local isodensity surfaces, as adopted by JS02. Since the shape of isodensity surface is sensitive to substructures around halos, the removal of substructures is required in this method. The goal of this paper is, however, to construct the PDF of projected non-sphericity of halos for observational applications. Since it is difficult to definitely remove the effect of substructures in real observations, we do not use isodensity surfaces in the later sections.

We note, however, that the fitting to isodensity surfaces yields similar results to the mass tensor $I = \sum xx$ after substructures are removed. Figure 2 shows the main halo of the same single-halo in top-left panel of Figure 1 *without substructures*. We also plot the projections of the two ellipsoids with the same mass determined by the mass tensor $I = \sum xx$ (green) and the isodensity surface $\rho = 100\rho_{\text{crit}}$

(red), where ρ_{crit} is the cosmic critical density. The two ellipsoids are similar, indicating that the fitting to isodensity surfaces is an effective method to determine A_k if substructures are removed.

Slightly different versions of mass tensors are also used in literature, including the following two;

$$\hat{I}_{\alpha\beta} = \sum_{i=1}^N \frac{x_{\alpha}^{(i)} x_{\beta}^{(i)}}{|\mathbf{x}^{(i)}|^2} \equiv \sum_i n_{\alpha}^{(i)} n_{\beta}^{(i)} \quad (4)$$

and

$$\tilde{I}_{\alpha\beta} = \sum_i \frac{x_{\alpha}^{(i)} x_{\beta}^{(i)}}{[R_e^{(i)}]^2} \equiv \sum_i \tilde{n}_{\alpha}^{(i)} \tilde{n}_{\beta}^{(i)}, \quad (5)$$

where

$$R_e^{(i)} = \left[\left(\frac{x_1^{(i)}}{A_1} \right)^2 + \left(\frac{x_2^{(i)}}{A_2} \right)^2 + \left(\frac{x_3^{(i)}}{A_3} \right)^2 \right]^{1/2} \quad (6)$$

is the ellipsoidal distance of the i -th particle.

To discuss the difference between the three mass tensors $I = \sum xx$, $\hat{I} = \sum nn$ and $\tilde{I} = \sum \tilde{n}\tilde{n}$, we consider a ‘‘self-similar’’ density distribution. Throughout this paper, we refer to the density distribution that is expressed by concentric ellipsoids with the same axis ratio and orientation as ‘‘self-similar’’ distribution.

For example, in the two-dimensional space, for a self-similar ellipse with axis lengths p and q , the two-dimensional counterparts of the mass tensors $I = \sum xx$, $\hat{I} = \sum nn$ and $\tilde{I} = \sum \tilde{n}\tilde{n}$ yield ellipses with axis ratio p/q , $\sqrt{p/q}$ and p/q , respectively. Although $\hat{I} = \sum nn$ can be used as an estimator of the non-sphericity of halos, it does not reproduce the axis ratio of isodensity surfaces even for a self-similar density distribution. In contrast, $\tilde{I} = \sum \tilde{n}\tilde{n}$ reproduces the isodensity surfaces of a self-similar density distribution. If the density distribution is not self-similar, however, the weighting by $R_e^{(i)}$ in Equation (5) becomes inappropriate for inner regions. Hence we adopt the mass tensor $I = \sum xx$, which is free from such a weighting scheme and reproduces the isodensity surfaces of a self-similar density distribution.

The definition of mass tensor varies with authors in the previous literature, and therefore the applied method of triaxial modelling in each study should be carefully noticed. For example, JS02 fitted ellipsoids to isodensity surfaces of their simulated halos. Also, the mass tensors $I = \sum xx$, $\hat{I} = \sum nn$, $\tilde{I} = \sum \tilde{n}\tilde{n}$ are considered by Despali et al. (2014), Ludlow et al. (2014) and Vega et al. (2016), respectively (although the results of Vega et al. (2016) are mainly based on $I = \sum xx$). We emphasize that these results should not be *quantitatively* compared unless the same method of triaxial modelling is applied.

3 Confrontation of EC Prediction against N-body Results

3.1 Ellipsoidal collapse model

Before presenting the comparison between EC and the N-body results, we briefly summarize the basic framework of EC (White & Silk 1979; Bond & Myers 1996). For definiteness, we adopt the notation by Rossi et al. (2011).

EC describes the evolution of a homogeneous ellipsoid, embedded with a tidal field. The tidal field is characterized by the eigenvalues of the tensor $\nabla_{ij}\phi/(4\pi G\bar{\rho}a^3)$, where ϕ , $\bar{\rho}$ and a denote the gravitational potential, the mean matter density, and the scale factor, respectively. The differentiation by ∇_{ij} is operated in the comoving coordinate system. We denote the eigenvalues of the tensor by λ_k ($k = 1, 2, 3$; $\lambda_1 \geq \lambda_2 \geq \lambda_3$).

In the linear regime, the density contrast δ is given by $\sum_k \lambda_k$, and λ_k , δ and ϕ grow in proportion to the linear growth rate $D(t)$. Therefore, at the initial time t_{ini} where the linear regime holds, the axis lengths of the ellipsoid A_k ($k = 1, 2, 3$) satisfy the following equations:

$$A_k(t_{\text{ini}}) = a(t_{\text{ini}})(1 - \lambda_k(t_{\text{ini}})) \quad (7)$$

and

$$\frac{dA_k(t_{\text{ini}})}{dt} = H(t_{\text{ini}}) \left[A_k(t_{\text{ini}}) - a(t_{\text{ini}})\lambda_k(t_{\text{ini}}) \frac{d \ln D}{d \ln a} \Big|_{t=t_{\text{ini}}} \right], \quad (8)$$

where $H(t)$ is the Hubble parameter.

Then the axis lengths A_k evolve according to the following equation of motion:

$$\begin{aligned} \frac{d^2 A_k(t)}{dt^2} = & \Omega_{\Lambda,0} H_0^2 A_k(t) \\ & - 4\pi G \bar{\rho}(t) A_k(t) \left[\frac{1 + \delta(t)}{3} + \frac{b'_k \delta(t)}{2} + \lambda'_{\text{ext},k}(t) \right]. \end{aligned} \quad (9)$$

The above equation of motion implies that the ellipsoid does not rotate with respect to the tidal field. Therefore the relation $A_3 \geq A_2 \geq A_1$ is conserved all the time since $\lambda_1 \geq \lambda_2 \geq \lambda_3$ at the initial time.

In the equation of motion (9), the interior tidal force b'_k within the ellipsoids is computed by

$$b'_k(t) = \prod_j A_j(t) \int_0^\infty \frac{d\tau}{(A_k^2(t) + \tau) \prod_j \sqrt{A_j^2(t) + \tau}} - \frac{2}{3}. \quad (10)$$

Also, the exterior tidal force $\lambda'_{\text{ext},k}$ is described by

$$\lambda'_{\text{ext},k}(t) = \frac{D(t)}{D(t_{\text{ini}})} \left[\lambda_k(t_{\text{ini}}) - \frac{\delta(t_{\text{ini}})}{3} \right]. \quad (11)$$

Equation (10) is the exact expression only for the homogeneous density as considered here. On the other hand, Equation (11) assumes the exact linear growth regime even when the later evolution may not be the case. Unlike $\lambda'_{\text{ext},k}$, the density contrast $\delta(t)$ is calculated at each time so that the mass

inside the ellipsoid $(4\pi\bar{\rho}/3)(1+\delta)A_1A_2A_3$ is constant. For the spherical case ($\lambda_1 = \lambda_2 = \lambda_3 = \delta_{\text{ini}}/3$ and $A_1 = A_2 = A_3 = R$), both b'_k and $\lambda'_{\text{ext},k}$ vanish, and the equation of motion simply reduces to $d^2R/dt^2 = \Omega_{\Lambda,0}H_0^2R - (4\pi/3)G\bar{\rho}(1+\delta)R$.

According to Equation (9), all the axis lengths A_k eventually collapse to zero, as in the spherical case. Therefore an additional assumption is needed to predict the eventual axis lengths A_k . In the spherical collapse model, it is conventionally assumed that the final (virial) radius r_{vir} and overdensity Δ_{vir} of a homogeneous sphere are computed from the virial theorem.

In the case of EC, however, there may be no widely accepted treatment of anisotropic virialization of different axes. In this paper, we adopt the one proposed by Bond & Myers (1996). They assumed each A_k *separately* stops collapsing when A_k reaches $a(t) \times (\Delta_{\text{vir}})^{-1/3}$, using the virial overdensity $\Delta_{\text{vir}}(z=0)$ in the *spherical* virial theorem. Such an ellipsoid corresponds to a halo which is virialized at $z=0$. For the current set of cosmological parameters, $\Delta_{\text{vir}} = 355.4$ and so $(\Delta_{\text{vir}})^{-1/3} = 0.144$.

In summary, EC describes the evolution of a homogeneous and isolated ellipsoid, based on the linear growth of density fluctuations. The treatment of the virialization is based on the non-trivial assumption that each axis separately virialize; the axis lengths A_k at low redshifts ($z \lesssim 1$) are determined mainly by this virialization criterion. In the next subsection, we compare the evolution of the individual simulated halos with the EC prediction on the object-wise basis for the first time.

3.2 Comparison of evolution of individual halos with EC prediction

On the basis of the ellipsoids defined via the mass tensor $I = \sum xx$ (Equation (3)), we compare the evolution of the individual simulated halos with the prediction of EC on the object-wise basis. For each FOF halo identified at $z=0$, we trace back the positions of the FOF member particles to each redshift. We then determine an ellipsoid of mass M_{FOF} at each redshift via the mass tensor $I = \sum xx$ by using all the particles including non-FOF particles. We first choose the center of the calculation of $I = \sum xx$ as that of the FOF member particles of the current halo at the corresponding redshift, and then perform the iteration until it is converged. Throughout this paper, we call the ellipsoids determined at $z \neq 0$ through the above procedure ‘‘protohalos’’ of each FOF halo. Note that the protohalos are *not* halos identified by the FOF algorithm at each redshift.

Figure 3 demonstrates the evolution of the single-halo in the top-left panel of Figure 1 ($M_{\text{FOF}} = 8.43 \times 10^{14} h^{-1} M_{\odot}$). The top-left panel shows the evolution of the axis lengths A_k of the protohalos enclosing $M_{\text{ellipsoid}} = M_{\text{FOF}}$ in units of their initial values at $z=99$. The axis lengths A_k determined by the mass tensor are plotted in filled squares; A_1 , A_2 and A_3 are plotted in red,

green and blue, respectively. The corresponding EC predictions are illustrated in solid and dotted lines with the same color as the simulation results. The solid lines adopt λ_k evaluated from A_k of the corresponding protohalo at $z = 99$ through Equation (7); $\lambda_k = 1 - A_k(1 - \delta_{\text{ini}}/3)/(A_1 A_2 A_3)^{1/3}$. On the other hand, the dashed lines identify λ_k with the eigenvalues of $\nabla_{ij}\phi/(4\pi G\bar{\rho}a^3)$ calculated from the top-hat smoothed density field at the scale $[3M_{\text{FOF}}/(4\pi\bar{\rho})]^{1/3}$, at the central position of the protohalo at $z = 99$. The difference between the solid and dashed lines implies that the EC prediction is somewhat sensitive to the initial conditions, but the two sets of lines are roughly the same.

The simulation results and the EC prediction agree at least approximately for $z > 9$. At around $z = 9$, however, the simulation results begin to deviate from the EC prediction. As shown in the top-right panel, the corresponding ellipticity (magenta open circle) becomes larger than the EC prediction (magenta thick line), even though the linear regime still holds at $z \sim 9$. The density distribution around the protohalo at $z = 9$ is shown in the middle-left panel, and the projections of the ellipsoids with mass $M_{\text{ellipsoid}}/M_{\text{FOF}} = 0.2, 0.4, 0.6, 0.8, 1$ are also plotted. The density distribution at $z = 9$ is almost homogeneous, and so the triaxial modelling of the density distribution is not easy.

In EC, Equation (10) assumes the density distribution inside the ellipsoid is homogeneous. Inside the simulated halo, however, the density distribution becomes highly inhomogeneous from $z = 3$ to $z = 1$, as shown in the middle-right and bottom-left panels; particles fall into the central region of the protohalo along filamentary structures, and the innermost region ($M_{\text{ellipsoid}} \lesssim 0.2M_{\text{FOF}}$) becomes highly denser. Due to the filamentary structures developed during these redshifts, the triaxial modelling is still a poor approximation of the density distribution. The inhomogeneity of density distribution is one of the reasons why the simulation results deviate from the EC prediction. In addition, the internal density distribution is far from self-similar; for example, the orientation of the inner ellipsoids at $z = 1$ is considerably different from the outer ones.

Nevertheless, the evolution of the axis lengths A_k very crudely follows the EC prediction up to the turn-around epoch ($z \sim 1$) as seen in the top-left panel. Given that the various simplifications of EC, even this level of agreement between the simulation and EC may be surprising.

After the turn-around epoch, however, the simulation results more strongly deviate from the EC prediction. For example, the major axis A_3 (blue squares) rapidly increases and then decreases after $z = 1$. Finally at $z = 0$, the ellipticity e is much larger than the EC prediction (top-right panel), although the triaxial modelling of the density distribution seems to work well at $z = 0$ (bottom-right panel). The five ellipsoids at $z = 0$ in the bottom-right panel are well aligned compared to $z = 1$, but the density distribution is still not self-similar; the innermost ellipsoid is tilted with respect to the outermost one, and inner ellipsoids are slightly more elongated than outer ones.

As another example, Figure 4 shows the results for another single-halo ($M_{\text{FOF}} = 3.44 \times$

$10^{14}h^{-1}M_{\odot}$). Similarly to the case of Figure 3, especially after the turn-around epoch, the simulation results substantially deviate from the EC prediction. As seen in the bottom and middle panels, the density distribution inside the halo is not self-similar, as well as the halo in Figure 3.

We have found that the difference between the simulation and EC strongly depends on individual halos. Basically, however, the EC prediction very roughly reproduces the simulation results up to the turn-around. After that, the difference between the simulation and EC becomes larger.

One might expect that the difference between the simulation results and the EC prediction is larger for a multiple-halo than a single-halo. We have found that, however, this is not necessarily the case; the individuality of the halos is more noticeable.

Actually, the difference between the model prediction and the simulation results is not peculiar to EC. In Suto et al. (2016), we compare the evolution of the spherical radius of individual simulated halos with the prediction of the spherical collapse model. We then showed that the spherical collapse model fairly well reproduce the evolution of the simulation results up to the turn-around epoch. After the turn-around epoch, however, the evolution of simulated halos deviates from the prediction of the spherical collapse model. In this subsection, it has turned out that EC does not improve the difference between simulations and theoretical models. This rather implies that the spherical assumption works surprisingly well despite the highly non-spherical structure and evolution of halos.

In Suto et al. (2016), we also showed the difference is mainly caused by the velocity dispersion developed after the turn-around epoch. In order to better understand the difference between the simulation results and the EC prediction, we focus on the evolution of the simulated halos *after the turn-around epoch* ($z \sim 1$). Because the difference between the simulation results and the EC prediction varies appreciably from halo to halo, we *statistically* compare them in the next section.

We note that several authors previously obtained the mean axis ratio of “protohalos” $\langle A_1/A_3 \rangle \sim 0.7$ at $z \sim 49$ (Porciani et al. 2002; Ludlow et al. 2014; Despali et al. 2014), while our “protohalos” have $\langle A_1/A_3 \rangle \sim 1$ at $z > 49$. This difference simply comes from the different definition of “protohalos”; the above authors defined a protohalo *solely* from particles that are destined to be members of an FOF halo identified at lower redshifts. As stated in Section 2.3, we calculate the mass tensor by using all the particles (*not only the FOF members*) within a sphere around the mass centroid, and the information from the FOF algorithm is used only for choosing the initial position of the mass centroid.

The definition of protohalos in simulations is not necessarily unique, and can be different depending on the aim of each study. Ludlow et al. (2014) noted that the axis ratio of their protohalos (positions of FOF members at $z_i=0$) significantly deviates from that expected from Equation (7). Thus they decided to adopt the initial axis ratio directly measured from their simulated protohalos, instead

of Equation (7), and to solve EC. By doing so, they found the better agreement between the EC model and simulations statistically. In contrast, we are interested in the individual evolution of each halo, and aim at identifying and clarifying when and how N-body simulations and the (standard) EC model deviate for the same initial condition. Hence we have defined our protohalos so that they satisfy the initial condition for A_k , i.e., Equation (7).

4 Evolution and Radial Profile of Axis Ratio

4.1 Evolution and mass dependence of non-sphericity of halos

One of the well-known discrepancies between EC and simulations is the mass dependence of ellipticity of halos at $z = 0$. Rossi et al. (2011) calculated EC for initial conditions described by the Gaussian random field and reported that more massive halos have smaller ellipticity in EC, while those in simulations have larger ellipticity at $z = 0$.

We examine the evolution of axis ratio A_1/A_3 and ellipticity e of our simulated halos. We have found that the initial $\lambda_k(z = 99)$ measured from the simulation precisely reproduces the prediction for the Gaussian random field; more massive protohalos have smaller ellipticity at $z = 99$. Also, more massive halos indeed have larger ellipticity on average at $z = 0$ in our simulation, as reported in the previous studies Jing & Suto (2002); Despali et al. (2014); Bonamigo et al. (2015); Vega et al. (2016). Therefore the dependence of the non-sphericity of the simulated halos on their mass has changed sometime before the present time.

Figure 5 demonstrates the mass dependence of axis ratio A_1/A_3 and ellipticity e at $z = 9, 1, 0.6, 0.2, 0$. Each symbol indicates A_1/A_3 or e of each halo; red circles are for single-halos ($M_2/M_1 < 0.2$) and green square are for multiple-halos ($M_2/M_1 > 0.2$). Note that, for $z \neq 0$, the results are for the protohalos of each FOF halo identified at $z = 0$.

The thick solid line illustrates the averaged value $\langle A_1/A_3 \rangle$ or $\langle e \rangle$ over all the simulated halos with the root-mean-square scatter shown in thin lines. We have found that $\langle A_1/A_3 \rangle$ and $\langle e \rangle$ only slightly change if we exclude the multiple-halos, although they are systematically less spherical than single-halos. This is because the fraction of the multiple-halos is small ($\sim 10\%$). The blue dashed line indicates the EC prediction from the initial condition λ_k calculated from A_k at $z = 99$ through Equation (7).

As shown in the top-left panel of Figure 5, at $z = 9$, more massive halos have larger A_1/A_3 both in EC and the simulation results, reflecting the tendency at the initial time. The large scatter for the symbols implies the strong individuality of halos, i.e., the mass dependence of axis ratio is clear only when it is seen *statistically*. The simulation results have systematically smaller values of A_1/A_3

than the EC prediction, implying that the axis ratio A_1/A_3 of the majority of individual halos deviate from the EC prediction even at around $z = 9$, as in the top-right panel of Figure 3.

At $z = 1$ (second-top panel), the mass dependence is preserved in EC, but it becomes weaker at small mass scales for the simulated halos. From $z = 0.6$ to $z = 0$ (bottom three panels), $\langle A_1/A_3 \rangle$ becomes gradually larger. The increase of A_1/A_3 is predicted by EC as in the top-right panels of Figures 3 and 4, although the values of A_1/A_3 are much different between EC and the simulation.

Most importantly, the mass dependence of $\langle A_1/A_3 \rangle$ of the simulated halos exhibits a clear *transition* after $z = 1$; the mass dependence becomes even weaker, and finally at $z = 0$, massive halos tend to be less spherical, opposite to that at the initial time. In contrast, the mass dependence of $\langle A_1/A_3 \rangle$ in EC is preserved from the initial time to the present time; massive halos are more spherical. The mass dependence of $\langle e \rangle$ exhibits a similar transition to $\langle A_1/A_3 \rangle$, as shown in the right panels of Figure 5. The redshift $z = 1$ corresponds, on average, to the turn-around epoch where the difference between the EC prediction and the evolution of individual halos becomes large (see Figures 3 and 4). We then expect that a similar transition of the mass dependence of $\langle A_1/A_3 \rangle$ or $\langle e \rangle$ occurs earlier at inner mass scales of the halos, since inner regions turn-around earlier than outer regions.

To confirm this, we compute the $A_k(M_{\text{ellipsoid}})$ at the mass scales $M_{\text{ellipsoid}} (< M_{\text{FOF}})$ for each halo. Figure 6 compares the evolution of $\langle A_1/A_3 \rangle$ and $\langle e \rangle$ at the three different mass scales $M_{\text{ellipsoid}} = M_{\text{FOF}}, M_{\text{FOF}}/2$ and $M_{\text{FOF}}/10$. The values of A_k are averaged over the three different mass ranges; heavy: $M_{\text{FOF}} > 2.5 \times 10^{14} h^{-1} M_{\odot}$ (green), intermediate: $1.25 \times 10^{14} h^{-1} M_{\odot} < M_{\text{FOF}} < 2.5 \times 10^{14} h^{-1} M_{\odot}$ (red) and light: $6.25 \times 10^{13} h^{-1} M_{\odot} < M_{\text{FOF}} < 1.25 \times 10^{14} h^{-1} M_{\odot}$ (black).

The top-left panel of Figure 6 illustrates the redshift evolution of $\langle A_1/A_3 \rangle$ at $M_{\text{ellipsoid}} = M_{\text{FOF}}$. At $z = 99$, massive halos tend to be less spherical. Keeping this tendency, $\langle A_1/A_3 \rangle$ decreases up to $z \sim 1$, corresponding to the turn-around epoch. After that, $\langle A_1/A_3 \rangle$ begins to increase and its mass dependence changes, as seen in Figure 5.

The middle-left and the bottom-left panels of Figure 6 show the results for the mass scales $M_{\text{ellipsoid}} = M_{\text{FOF}}/2$ (middle) and $M_{\text{FOF}}/10$ (bottom), respectively. As seen in Figure 6, more massive halos become less spherical at $z \sim 1$. At $M_{\text{ellipsoid}} = M_{\text{FOF}}/2$ and $M_{\text{ellipsoid}} = M_{\text{FOF}}/10$, a similar change in the mass dependence of $\langle A_1/A_3 \rangle$ occurs at $z \sim 2$ and $z \sim 4$, respectively. Indeed, the mass dependence of $\langle A_1/A_3 \rangle$ changes earlier at inner mass scales. Similar things occur also in the mass dependence of $\langle e \rangle$, as shown in the right panels of Figure 6.

The redshift where the mass dependence of $\langle A_1/A_3 \rangle$ and $\langle e \rangle$ changes roughly corresponds to the turn-around epoch for each mass scale. Hence the change in the mass dependence of $\langle A_1/A_3 \rangle$ is associated with the virialization process after the turn-around. We then suspect that the change in the mass dependence may be related to the development of the velocity dispersion after the turn-around

epoch. Hence we examine the radial profile of the velocity dispersion after $z = 1$ and compare it with the radial profiles of $\langle A_1/A_3 \rangle$ and $\langle e \rangle$ in the next subsection.

4.2 Radial profile of axis ratio inside FOF halos and the origin of the mass dependence of axis ratio

Figure 7 shows the radial profiles of the radial velocity dispersion σ_r^2 and the “velocity isotropy measure” defined by $(\sigma_\theta^2 + \sigma_\phi^2)/(2\sigma_r^2)$ at $z = 1, 0.8, 0.6, 0.4, 0.2, 0.1, 0$ (after the turn-around epoch). We here use spherical mass coordinate M_{sphere} for simplicity, and calculate each component of velocity dispersion in the spherical coordinate. In the left panel, the radial velocity dispersion σ_r^2 is normalized by the circular velocity $v_{\text{circ}}^2(M_{\text{FOF}})$ at $M_{\text{sphere}} = M_{\text{FOF}}$:

$$v_{\text{circ}}^2(M_{\text{FOF}}) = \frac{GM_{\text{FOF}}}{R_{\text{FOF}}}, \quad (12)$$

where R_{FOF} is the radius of the sphere enclosing the mass M_{FOF} . We first compute the radial profiles of $\sigma_r^2/v_{\text{circ}}^2$ and $(\sigma_\theta^2 + \sigma_\phi^2)/(2\sigma_r^2)$ for an individual halo, and then average further the radial profiles over the 2004 halos to obtain the “mean” radial profiles, $\langle \sigma_r^2/v_{\text{circ}}^2 \rangle$ and $s \equiv \langle (\sigma_\theta^2 + \sigma_\phi^2)/(2\sigma_r^2) \rangle$. Note that, for $z \neq 0$, the results are for the protohalos of each FOF halo identified at $z = 0$. We have confirmed that the radial profiles in Figure 7 are almost unchanged even if we include/exclude the multiple-halos.

The left panel of Figure 7 indicates that the radial velocity dispersion $\langle \sigma_r^2/v_{\text{circ}}^2 \rangle$ is larger at the innermost regions at every redshift. At around $M_{\text{sphere}} = M_{\text{FOF}}$, σ_r^2 rapidly decreases and becomes roughly constant at outer regions. The small values of $\langle \sigma_r^2/v_{\text{circ}}^2 \rangle$ at outer regions can be attributed to the particles coherently falling toward the central region with small radial velocity dispersion.

In the right panel of Figure 7, the averaged radial profile of the velocity isotropy measure s at each redshift has roughly three different regions. At the innermost region, s is approximately unity, indicating that the velocity is almost isotropic. At around $M_{\text{sphere}} = M_{\text{FOF}}$, s rapidly increases, corresponding to the decrease of $\langle \sigma_r^2/v_{\text{circ}}^2 \rangle$ in the left panel. Then s reaches a maximum. We indicate the maximum point by an arrow in the figure. Outside the maximum point, s slowly decreases.

We indicate the location where the velocity isotropy measure s reaches the maximum by an arrow also in the left panel. At this location, the radial profile of $\langle \sigma_r^2/v_{\text{circ}}^2 \rangle$ becomes roughly flat. We find that this location very roughly corresponds to the “splash-back radius” r_{sb} (Adhikari et al. 2014; Diemer & Kravtsov 2014; More et al. 2015), although their agreement strongly depends on individual halos. We note that r_{sb} moves outward with time, indicating that the velocity dispersion develops and extends outward. We next examine how the radial profiles of the axis ratio $\langle A_1/A_3 \rangle$ and $\langle e \rangle$ behaves inside and outside r_{sb} .

Figure 8 illustrates the radial profiles of axis ratio $\langle A_1/A_3 \rangle$ and ellipticity $\langle e \rangle$ averaged over

our 2004 halos for $z = 1, 0.8, 0.6, 0.4, 0.2, 0.1, 0$. The horizontal axis $M_{\text{ellipsoid}}$ indicates the mass of ellipsoids determined by the mass tensor $I = \sum xx$ using internal and external density distributions for each halo. We refer to the sequence of $\langle A_1/A_3 \rangle$ or $\langle e \rangle$ of such ellipsoids as “radial profiles”. Note that the central position differs from inner to outer ellipsoids belonging to the same FOF halo (see bottom panels of Figures 3 and 4). We have confirmed that the radial profiles in Figure 8 are almost unchanged even if we include/exclude the multiple-halos.

The left panel of Figure 8 shows the evolution of the radial profile of $\langle A_1/A_3 \rangle$. At least after $z \sim 0.4$, the radial profile of $\langle A_1/A_3 \rangle$ rapidly decreases beyond a certain mass scale around $M_{\text{ellipsoid}} \sim M_{\text{FOF}}$. Similarly, as shown in the right panel of Figure 8, the profile of ellipticity $\langle e \rangle$ rapidly increases there. This corresponds to the development of filamentary structures surrounding the halos (cf. the bottom-left panel of Figure 3). The characteristic mass scale moves outward with time, and eventually becomes larger than M_{FOF} after $z \lesssim 0.4$.

We indicate the location where the velocity isotropy measure s reaches a maximum, roughly corresponding to the splash-back radius r_{sb} , at each redshift by an arrow in both panels of Figure 8. The characteristic mass scale in the radial profile of $\langle A_1/A_3 \rangle$ or $\langle e \rangle$ roughly corresponds to r_{sb} , given that M_{sphere} is not exactly identical to $M_{\text{ellipsoid}}$. These two mass scales may give a rough indication of the physical boundary of halos inside which the velocity dispersion has been developed.

Figures 5 to 8 imply that the mass dependence of axis ratio $\langle A_1/A_3 \rangle$ changes almost simultaneously the velocity dispersion $\langle \sigma_r^2/v_{\text{circ}}^2 \rangle$ becomes larger. We note, however, that the halos have a significant mean ellipticity $\langle e \rangle$ inside the splash-back radius r_{sb} . This may seem inconsistent with the fact that the velocity dispersion is almost isotropic at the innermost region (Figure 7). Hence some unknown mechanism other than the velocity anisotropy is needed to maintain the highly non-spherical density distribution of the halos, which remains as a puzzle.

We have adopted a simple version of EC. In contrast, several authors have proposed to refine EC, for instance, by a better mapping between the current halos and their corresponding ancestors at earlier epochs (Borzyszkowski et al. 2014; Ludlow et al. 2014), and by using a different empirical treatment of the virialization (Angrick & Bartelmann 2010). While those approaches improve the agreement between the EC predictions and simulation results to some extent, they require additional ad-hoc assumptions, and are not necessarily satisfactory. Thus we do not consider the modification of the EC model, but conclude that the predictions of EC are not so robust, and that quantitative predictions of non-sphericities of clusters in precision cosmology era should be made via numerical simulations.

Hence we move on to detailed analyses of simulation results in the next section. Especially, we pay a special attention to the radial dependence of $\langle A_1/A_3 \rangle$ and $\langle e \rangle$ in Figure 8. While inner

regions are more spherical at $z = 1$, inner regions are less spherical at $z = 0$. This radial dependence may seem small, but indicates that the halos are not self-similar. We examine how the probability distribution function of A_1/A_3 depends on $M_{\text{ellipsoid}}$ in the next section.

5 Probability Distribution Function of Axis Ratio

5.1 Minor-to-major axis ratio of triaxial ellipsoids

Previously, JS02 measured the minor-to-major axis ratio A_1/A_3 of the isodensity surface at $\rho = 2500\rho_c$ (approximately corresponding to $0.3 r_{\text{vir}}$) of their simulated halos. They further assumed the self-similarity of the density distribution inside the halos, and obtained the following fitting formula at the virial mass M_{vir} :

$$P(A_1/A_3; M_{\text{vir}}, z) = \frac{1}{\sqrt{2\pi}0.113} \left(\frac{M_{\text{vir}}}{M_*} \right)^{0.07\Omega_m(z)^{0.7}} \times \exp \left[\frac{[(A_1/A_3)(M_{\text{vir}}/M_*)^{0.07\Omega_m(z)^{0.7}} - 0.54]^2}{2(0.113)^2} \right], \quad (13)$$

where $M_*(z)$ is the characteristic non-linear mass scale. The scale is determined so that the top-hat smoothed mass fluctuation $\sigma(M_*, z)$ becomes $\delta_c = 1.68$, where δ_c is the linearly-extrapolated critical density contrast in the spherical collapse model.

In the previous section, however, we have seen that the axis ratio $A_1/A_3(M_{\text{ellipsoid}})$ is not constant as a function of $M_{\text{ellipsoid}}$ (Figure 8). This result implies that the formula (13) may not be reliable since it is based on the self-similarity assumption. Therefore, we here quantitatively show the extent to which the departure from self-similarity affects the probability distribution function (PDF) of A_1/A_3 .

Figure 9 illustrates the PDFs of axis ratio A_1/A_3 of our 2004 halos, determined by $I = \sum xx$ at the three different mass scales $M_{\text{ellipsoid}} = M_{\text{FOF}}$, $M_{\text{FOF}}/2$ and $M_{\text{FOF}}/10$. The simulated halos are classified into three categories according to the mass of the most massive substructure M_2 compared to that of the main halo M_1 ; $M_2/M_1 < 0.1$ (red), $0.1 < M_2/M_1 < 0.2$ (blue), $M_2/M_1 > 0.2$ (green). The red and blue portions correspond to the single-halos defined in Section 2.2, and the green portion corresponds to the multiple-halos.

The bottom panel of Figure 9 shows the result for $M_{\text{ellipsoid}} = M_{\text{FOF}}/10$, approximately corresponding to the region enclosed by the isodensity surface $\rho = 2500\rho_c$. The PDF of our halos is shifted to the left compared to Equation (13). Their difference may be partly explained by the different methods of triaxial modelling of halos; the mass tensor and the isodensity surfaces.

As shown in the middle panel of Figure 9, the PDF of A_1/A_3 for $M_{\text{ellipsoid}} = M_{\text{FOF}}/2$ is shifted to the right compared with that of $M_{\text{FOF}}/10$. Hence the region at $M_{\text{ellipsoid}} = M_{\text{FOF}}/2$ inside the halos

is, on average, more spherical than $M_{\text{FOF}}/10$, corresponding to the radial profiles of A_1/A_3 and e in Figure 8. Similarly, as shown in the top panel, the region $M_{\text{ellipsoid}} = M_{\text{FOF}}$ is even more spherical, clearly indicating that the PDF of A_1/A_3 depends on $M_{\text{ellipsoid}}$ due to the non-self-similarity of halos. Quantitatively, the mean value $\langle A_1/A_3 \rangle$ at $M_{\text{ellipsoid}} = M_{\text{FOF}}/2$ and $M_{\text{ellipsoid}} = M_{\text{FOF}}/10$ is smaller by $\sim 10\%$ and $\sim 15\%$ than that at $M_{\text{ellipsoid}} = M_{\text{FOF}}$.

For $M_{\text{ellipsoid}} = M_{\text{FOF}}$, the PDF of our halos is similar to Equation (13), except for the fraction by the multiple-halos. This is most likely just a coincidence; the difference in A_k by the mass tensor and the isodensity surfaces, and the radial profile of A_1/A_3 are accidentally compensated. At $M_{\text{ellipsoid}} = M_{\text{FOF}}/2$ and M_{FOF} , the multiple-halos are significantly less spherical than single-halos. In contrast, the multiple-halos do not have such a tendency at $M_{\text{ellipsoid}} = M_{\text{FOF}}/10$. This is because the multiplicity of halos is determined by the amount of substructures with all the FOF members; For example, the region of $M_{\text{FOF}}/10$ of a halo comprising two comparable mass objects may include only one of them.

Previously, Vega et al. (2016) calculated the PDF of A_1/A_3 of their simulated halos at the two different mass scales $M_{\text{ellipsoid}} \approx M_{\text{FOF}}$ and $M_{\text{ellipsoid}} \approx M_{\text{FOF}}/2$ *without* the self-similarity assumption. They then found that $\langle A_1/A_3 \rangle$ at the inner mass scale is smaller by $\sim 10\%$ than that at the outer mass scale. This is consistent with our results, although their methods of triaxial modelling and halo identification are slightly different from ours.

In observations, since the density distribution of halos is projected on the sky, the PDF of projected axis ratio is more relevant in interpreting observational data. In fact, OLS03 calculated the PDF of projected axis ratio by integrating imaginary halos whose axis lengths A_k follow the formula (13). The scale dependence of the PDF of A_1/A_3 indicates that the self-similar assumption is not valid when constructing a PDF of projected axis ratio through a PDF of A_1/A_3 , as employed previously (e.g., OLS03; Kawahara 2010). Therefore, we instead directly measure the projected axis lengths by projecting the density distribution of the simulated halos in the next subsection.

5.2 Axis ratio from projected density distribution

Figure 10 (a) shows the histograms of the projected axis ratio of our halos at $z = 0$. Instead of M_{FOF} , $M_{\text{FOF}}/2$, $M_{\text{FOF}}/10$ in Figure 9, we measure three observationally more relevant mass scales; M_{vir} , M_{500} and M_{2500} . The virial mass M_{vir} is defined as the mass of the sphere within which the averaged overdensity becomes $\Delta_{\text{vir}}(z = 0) = 355.4$ times cosmic mean matter density, and M_{500} and M_{2500} are the masses of the sphere within which the mean density is 500 and 2500 times the cosmic critical density. Actual lensing halos are observed roughly up to the scale of M_{500} . Typically, $M_{500} \sim 0.5M_{\text{vir}}$

and $M_{2500} \sim 0.2M_{\text{vir}}$. In reality, these mass scales are measured from the projected density distribution on the sky, but here we determine them in the three-dimensional space for simplicity.

We determine an ellipse by using the two dimensional counterpart of $I = \sum xx$ from the projected density distributions of each halo along the x -, y - and z -axes of our simulation. We choose a rectangular box with the depth only along the line-of sight confined so that the region barely encloses all the FOF member particles. Therefore we consider all the particles in the box, but neglect the contribution from foreground and background particles outside the box. The particle number N in Equation (3) is set so that the (projected) mass inside the ellipse becomes any of M_{vir} , M_{500} and M_{2500} . We call the axis lengths of the resulting ellipse a_1 and a_2 ($a_1 < a_2$). Note that we obtain three values of a_1/a_2 for each halo.

The top panel of Figure 10 (a) shows the histogram for M_{vir} ($\approx M_{\text{FOF}}$) at $z = 0$. The histogram is separately colored by single-halos ($M_2/M_1 < 0.2$) and multiple-halos ($M_2/M_1 > 0.2$). Due to the projection effect, the overall shape of the histogram is broader and more shifted to the right (rounder) than that of A_1/A_3 for M_{FOF} in Figure 9. Also, compared to A_1/A_3 , the portion of the multiple-halos in the PDF is extended to the right; if two major components of a multiple-halo are along the line-of-sight, it may be regarded a single object from an observer.

We find that the histogram of projected axis ratio is well approximated by the beta distribution:

$$P(x; a, b) = \frac{x^{a-1}(1-x)^{b-1}}{B(a, b)}, \quad (14)$$

where

$$B(a, b) = \int_0^1 x^{a-1}(1-x)^{b-1} dx \quad (15)$$

is the beta function and a and b are parameters. The mean μ and the variance σ^2 of the beta distribution are given by

$$\mu = \frac{a}{a+b}, \quad \sigma^2 = \frac{ab}{(a+b)^2(a+b+1)}, \quad (16)$$

respectively. Table 2 lists the parameters a and b along with the mean value and the standard deviation calculated from a and b . The values of mean μ and variance σ^2 do not change much even when we include/exclude the multiple-halos. Such weak dependence on the multiplicity of halos is useful when the fitting formula is compared with real observational data, since it is difficult to determine the multiplicity of real halos, and to remove substructures in observations.

Our result should be compared with the PDF of a_1/a_2 by OLS03 that integrates the PDF of A_1/A_3 by JS02. We emphasize that the PDF of OLS03 is sensitive to the self-similarity assumption by JS02. When calculating the PDF of OLS03, we substitute $M_{\text{vir}} = 2 \times 10^{14} h^{-1} M_{\odot}$ in Equation (13), corresponding to the mean mass of our sample. The PDF of OLS03 is plotted in blue dashed

curve in Figure 10. Since the PDF of A_1/A_3 for $M_{\text{FOF}}(\approx M_{\text{vir}})$ well follows the model of JS02 by coincidence (the top-panel of Figure 9), the difference between OLS03 and the histogram is mainly due to the self-similarity assumption for the density distribution inside halos, adopted by JS02 and OLS03. This difference clearly demonstrates the importance of the projection effect.

The middle and bottom panels of Figure 10 (a) show the histograms for M_{500} and M_{2500} , respectively, compared with OLS03. Since OLS03 assumes the self-similarity of density distribution, the blue-dashed curves in the three panels of Figure 10 (a) are the same. These histograms show that the inner region is slightly less spherical than the outer region. This dependence is similar to the case of A_1/A_3 (Figure 9), but significantly weaker due to the projection.

The PDF of a_1/a_2 at M_{500} and M_{2500} are also well approximated by the beta distribution, and the best-fit parameters are listed in Table 2. It may seem that, for M_{2500} , the PDF of OLS03 is in better agreement in the simulation results. Given that the significant difference in the bottom panel of Figure 9 at $M_{\text{FOF}}/10$, however, this is also just a coincidence, and rather implies the importance of the projection effect for non-self-similar halos.

We repeat the same analysis for $z = 0.2, 0.4$ and 1 . In doing so, we find halos by the FOF algorithm *at each redshift separately*; in the preceding sections, we have traced back the evolution of protohalos of each FOF halo identified at $z = 0$, which does not correspond to real observational situations because observed halos are defined at each z . The multiplicity of the halos is also defined at each redshift, according to the mass of the most massive substructure M_2 relative to that of the main halo M_1 . In addition, we extract halos with $M_{\text{FOF}} > 6.25 \times 10^{13} h^{-1} M_{\odot}$ at each redshift. Hence the number of the halos depends on redshift, and is indicated in Figure 10 and Table 2. Note that the virial overdensity $\Delta_{\text{vir}}(z)$ depends on redshift; e.g., $\Delta_{\text{vir}}(z = 1) = 203.2$.

Figure 10 (b), (c) and (d) show the results for halos at higher redshifts; $z = 0.2, 0.4$ and 1 , respectively. For each redshift, the PDF of OLS03 (blue curves) in the three panels are the same, but it slightly differs with redshift. The result for every redshift is basically similar to $z = 0$. Also, all the histograms are well approximated by the beta distribution (Equation (14)) and best-fit parameters are listed in Table 2.

According to Table 2, The mean value also has weak redshift dependence; it becomes smaller toward earlier redshifts. This is partly due to the fixed minimum mass for the sets of halos at different redshifts. At earlier redshifts, more massive fraction is chosen out of all the halos, so the mean axis ratio becomes smaller.

We have found that the values of mean and standard deviation of a_1/a_2 calculated directly from the simulation results agree within 5 % from those in Table 2. In addition, the dependence of the mean value on mass scale and redshift are the same as discussed above, implying the goodness of

| | | all halos | | | | single-halos only | | | |
|---------------------|------------------|-----------|------|------|------|-------------------|------|------|------|
| | | a | b | mean | s.d. | a | b | mean | s.d. |
| $z = 0$ | M_{vir} | 4.18 | 2.71 | 0.61 | 0.17 | 5.00 | 2.99 | 0.63 | 0.16 |
| $N = 2004 \times 3$ | M_{500} | 4.01 | 2.90 | 0.58 | 0.18 | 4.32 | 2.98 | 0.59 | 0.17 |
| | M_{2500} | 4.35 | 3.39 | 0.56 | 0.17 | 3.92 | 3.14 | 0.56 | 0.17 |
| $z = 0.2$ | M_{vir} | 4.01 | 2.81 | 0.59 | 0.18 | 4.83 | 3.13 | 0.61 | 0.16 |
| $N = 1550 \times 3$ | M_{500} | 3.69 | 2.92 | 0.56 | 0.18 | 4.18 | 3.13 | 0.57 | 0.17 |
| | M_{2500} | 4.34 | 3.65 | 0.54 | 0.17 | 4.46 | 3.74 | 0.54 | 0.16 |
| $z = 0.4$ | M_{vir} | 4.02 | 3.03 | 0.57 | 0.17 | 4.78 | 3.34 | 0.59 | 0.16 |
| $N = 1101 \times 3$ | M_{500} | 3.72 | 3.11 | 0.54 | 0.18 | 4.26 | 3.38 | 0.56 | 0.17 |
| | M_{2500} | 4.21 | 3.69 | 0.53 | 0.17 | 3.82 | 3.32 | 0.54 | 0.17 |
| $z = 1$ | M_{vir} | 3.40 | 2.74 | 0.55 | 0.19 | 4.45 | 3.33 | 0.57 | 0.17 |
| $N = 317 \times 3$ | M_{500} | 3.22 | 2.83 | 0.53 | 0.19 | 3.89 | 3.25 | 0.54 | 0.17 |
| | M_{2500} | 3.93 | 3.80 | 0.51 | 0.17 | 3.95 | 3.77 | 0.51 | 0.17 |

Table 2. List of the parameters of the beta distribution (14) that approximates the PDF of projected axis ratio for M_{vir} , M_{500} and M_{2500} for four redshifts. The mean $\mu = a/(a+b)$ and the standard deviation $\sigma = \sqrt{ab/[(a+b)^2(a+b+1)]}$ of the beta distribution are also shown.

the fitting by the beta distribution.

In addition, the statistical mass dependence of a_1/a_2 is also weak. Figure 11 shows the axis ratio a_1/a_2 of each halo against its M_{vir} (left panel) and M_{500} (right panel). Except for the most massive part where the number of halos is small, the mass dependence of a_1/a_2 is even weaker than the three-dimensional axis ratio A_1/A_3 plotted in Figure 5. Therefore the minimum mass $M_{\text{vir}} = 6.25 \times 10^{13} h^{-1} M_{\odot}$ set in the above analysis is not so critical. The weak dependence of the PDF of a_1/a_2 on redshift, mass scales (M_{vir} , M_{500} , M_{2500}) and the minimum mass of the halos are useful when the model is compared with observational data.

5.3 Comparison with observational sample

As an example of possible applications of our fitting formula for the PDF of projected axis ratio a_1/a_2 , we attempt to compare it with the PDF for the observed halos estimated by Oguri et al. (2010). They measured the projected axis ratio from the weak lensing shear map of 18 clusters. In doing so, they assumed that the three-dimensional density distribution inside each halo follows a self-similar triaxial ellipsoid. The observed region of their clusters roughly corresponds to M_{500} , and their mean redshift is 0.23, so we compare their observation data with our model for M_{500} of all the halos and $z = 0.2$ in

Table 2. The mean virial mass M_{vir} of our sample is roughly $2 \times 10^{14} h^{-1} M_{\odot}$.

The left panel of Figure 12 plots the PDF of projected axis ratio of the observed halos in red symbols with error bars. Oguri et al. (2010) compared this observational results with the PDF of OLS03 calculated by assuming $M_{\text{vir}} = 7 \times 10^{14} h^{-1} M_{\odot}$ in Equation (13), corresponding to the mean mass of the observed clusters. We also plot the same PDF in the blue curve. In addition, our model is plotted in the black curve. The mean mass of our sample is smaller than that of Oguri et al. (2010), but this is not serious since the mass dependence of axis ratio a_1/a_2 is very weak (Figure 11).

In order to include the possible effect of the observational uncertainty in a_1/a_2 , Oguri et al. (2010) convolved the PDF of OLS03 with the Gaussian function with $\sigma = 0.15$, corresponding to the typical uncertainty of the measurement of the axis ratio (cf. Table 1 of Oguri et al. (2010)). We repeated the same procedure for the PDF of OLS03 and our fitting formula.

The resulting PDFs are plotted in the right panel of Figure 12. Because of the large observational error bars, it is difficult to distinguish the PDF of OLS03 and our fitting formula. Our fitting formula is, however, based on the direct measurement of a_1/a_2 of the simulated halos, and therefore more reliable than that of OLS03 based on the self-similarity of halos. In the near future, precise observational data of numerous clusters will be provided by Subaru Hyper Suprime-Cam, for example. In order to perform much more precise comparison of observational data and theory, one should adopt the same estimator of the projected axis lengths both for observations and simulations. Hence more elaborate analyses will be a useful tool to test the non-sphericity of halos predicted in the CDM cosmology. Our current results are indeed towards such a purpose.

6 Summary and Discussion

We have studied the redshift evolution, and the mass- and radial-dependence of non-sphericity by analyzing halos from a cosmological N-body simulation. We approximated the density distribution of the halos by triaxial ellipsoids, employing the mass tensor $I = \sum xx$ (Equation (3)). Our major findings are summarized as follows.

1. For the first time, we compared the evolution of the axis lengths A_k ($k = 1, 2, 3$) of the triaxial ellipsoids of individual simulated halos with the prediction of the ellipsoidal collapse model (EC) *on the object-wise basis*. In general, the EC prediction roughly reproduces the simulation up to the turn-around epoch ($z \sim 1$). After the turn-around epoch, however, the simulation substantially deviates from the EC prediction.
2. The discrepancy in the statistical mass dependence of axis ratio A_1/A_3 at $z = 0$ between the EC prediction and simulations has been reported in literature; massive halos are more spherical in EC,

but those in simulations tend to be less spherical. For the first time, we demonstrated how and when the statistical mass dependence of A_1/A_3 of the simulated halos deviates from EC. While massive halos are more spherical initially, they gradually become less spherical after the turn-around epoch. This tendency is opposite to the EC prediction.

3. The averaged axis ratio $\langle A_1/A_3 \rangle$ over all the simulated halos has significant radial dependence as a function of enclosed mass $M_{\text{ellipsoid}}$. At $M_{\text{ellipsoid}} \gtrsim M_{\text{FOF}}$, $\langle A_1/A_3 \rangle$ rapidly decreases due to filamentary structures around the halos. Inside $M_{\text{ellipsoid}} \sim M_{\text{FOF}}$, the radial dependence of $\langle A_1/A_3 \rangle$ gradually changes with time; while $\langle A_1/A_3 \rangle$ increases toward the inner region at $z = 1$, it decreases at $z = 0$. The radial dependence of $\langle A_1/A_3 \rangle$ indicates that the halos are not necessarily self-similar (concentric, common axis ratio and orientation).
4. We examined how the probability distribution function (PDF) of A_1/A_3 of triaxial halos at $z = 0$ depends on $M_{\text{ellipsoid}}$. The values of $\langle A_1/A_3 \rangle$ at $M_{\text{ellipsoid}} = M_{\text{FOF}}/10$ is smaller than that of JS02 who employ the isodensity surface at $\rho = 2500\rho_{\text{crit}}$ (roughly corresponding to the region of $M_{\text{FOF}}/10$) and adopt the self-similarity assumption. The difference is partly due to the different methods of triaxial modelling of halos; mass tensor and isodensity surface.
5. The projected axis ratio a_1/a_2 is a more relevant quantity to compare with observational data, and we find that it is sensitive to the self-similarity assumption as well. Therefore we calculated the PDF of a_1/a_2 , not through those of three-dimensional A_1/A_3 , but directly from the projected density distributions of the simulated halos for the first time. We provide a fitting formula for the resulting PDF, and show that the formula improves those in previous studies that assume the self-similarity of halos. Hence our fitting formula will play important roles in interpreting the future data of Subaru Hyper Suprime-Cam among others.

Our current analysis is based on the dark-matter only simulation, which is reasonably justified in applying to weak-lensing observations. In a complementary fashion, X-ray observations of intra-cluster gas provide independent information on the non-sphericity of clusters. The density distribution of gas is, however, not necessarily identical to that of dark matter (Lee & Suto 2003; Kawahara 2010). Therefore, in order to study the non-sphericity of the gas density distribution without additional assumptions like hydrostatic equilibrium, hydrodynamical simulations including gas are needed. This is what we are currently working on, and will be presented elsewhere.

Acknowledgements

We thank an anonymous referee for many valuable comments. We gratefully acknowledge fruitful discussions with Benedikt Diemer, Hajime Kawahara, Surhud More, Masamune Oguri and Sébastien Peirani. This work is supported partly by JSPS Core-to-Core Program "International Network of Planetary Sciences", and by JSPS Grant-in-Aid for Scientific Research No. 26-11473 (D.S.), No. 25400236 (T. K.) and No. 24340035 (Y. S.). The numerical simulation in this work was carried out on Cray XC30 at Center for Computational Astrophysics, CfCA, of National Astronomical Observatory of Japan.

References

- Adhikari, S., Dalal, N. & Chamberlain, R. T., 2014, JCAP, 11, 019
- Angrick, C. & Bartelmann, M., 2010, A&A, 518, A38
- Bardeen, J. M., Bond, J. R., Kaiser, N. & Szalay, A. S., 1986, ApJ, 304, 15
- Bonamigo, M., Despali, G., Limousin, M. et al., G., 2015, MNRAS, 449, 3171
- Bond, J. R., Myers, S. T., 1996, ApJS, 103, 1
- Borzyszkowski, M., Ludlow, A. D., & Porciani, C., 2014, MNRAS, 445, 4124
- Bryan, S. E., Kay, S. T., Duffy, A. R. et al., 2013, MNRAS, 429, 3316
- Butsky, I., Macciò, A. V., Dutton, A. A. et al., 2015, arXiv:1503.04814
- Crocce, M., Pueblas, S., & Scoccimarro, R., 2006, MNRAS, 373, 369
- Davis, M., Efstathiou, G., Frenk, C. S., & White, S. D. M., 1985, ApJ, 292, 371
- Despali, G., Tormen, G., & Sheth, R., K., 2013, MNRAS, 431, 1143
- Despali, G., Giocoli, C. & Tormen, G., 2014, MNRAS, 443, 3208
- Diemer, B. & Kravtsov, A., V., 2014, ApJ, 789, 1
- Doroshkevich, A. G., 1970, Astrofizika, 6, 581
- Gunn, J. E., 1977, ApJ, 218, 592
- Gunn, J. E., Gott, J. R., III, 1972, ApJ, 176, 1
- Hinshaw, G., Larson, D., Komatsu, E., et al., 2013, ApJ, 208, 19
- Jing, Y. P., Suto, Y., 2002, ApJ, 574, 538 (JS02)
- Kawahara, H., 2010, ApJ, 719, 1926
- Lee, J., & Suto, Y. 2003, ApJ, 585, 151
- Lewis, A., Challinor, A., & Lasenby, A., 2000, ApJ, 538, 473
- Ludlow, A. D. & Porciani, C., 2011, MNRAS, 413, 1961
- Ludlow, A. D., Borzyszkowski, M. & Porciani, C., 2014, MNRAS, 445, 4110

More, S., Diemer, B. & Kravtsov, A. V., 2015, *ApJ*, 810, 36
Nakamura, T. T. & Suto, Y., 1997, *Prog. Theor. Phys.*, 97, 49
Nishimichi, T. Shirata, A., Taruya, A. et al., 2009, *PASJ*, 61, 321
Nishimichi, T. & Oka, A., 2014, *MNRAS*, 444, 1400
Oguri, M., Lee, J. & Suto, Y., 2003, *ApJ*, 599, 7 (OLS03)
Oguri, M., Takada, M., Okabe, N., & Smith, G. P., 2010, *MNRAS*, 405, 2215
Peebles, P. J. E., 1980, *Large-Scale Structure of the Universe* (Princeton: Princeton Univ. Press)
Porciani, C., Dekel, A. & Hoffman, Y., 2002, *MNRAS*, 332, 339
Press, W. H. & Schechter, P., 1974, *ApJ*, 187, 425
Rossi, G., Sheth, R. K. & Tormen, G., 2011, *MNRAS*, 416, 248
Schneider, M. D., Frenk, C. S. & Cole, S., 2012, *JCAP*, 5, 30
Scoccimarro, R., 1998, *MNRAS*, 299, 1097
Sheth, R. K., Tormen, G., 2002, *MNRAS*, 329, 61
Springel, V., 2005, *MNRAS*, 364, 1105
Springel, V., White, S. D. M., Tormen, G., & Kauffmann, G., 2001, *MNRAS*, 328, 726
Suto, D., Kitayama, T., Osato, K., Sasaki, S. & Suto, Y., 2016, *PASJ*, 68, 14
Valageas, P., Nishimichi, T., 2011, *A&A*, 527, 87
Velliscig, M., Cacciato, M., Schaye, J. et al., 2015 *MNRAS*, 453, 721
Vega, J., Yepes, G. & Gottlöber, S., 2016, arXiv:1603.02256
White, S. D. M. & Silk, J., 1979 *ApJ*, 231, 1

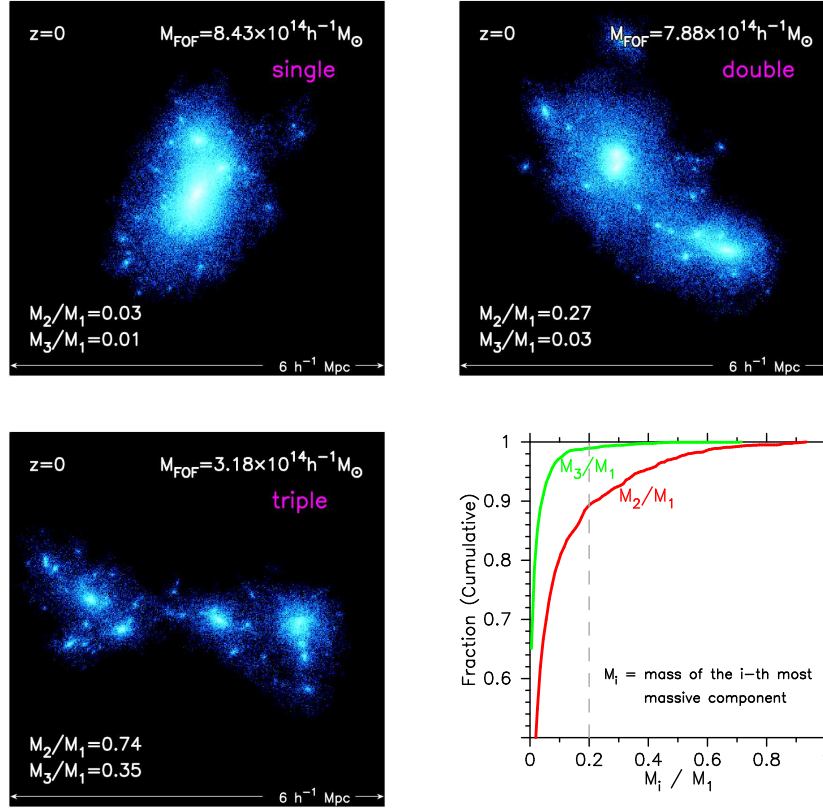


Fig. 1. Examples of morphology of dark matter halos. The upper panels and the lower-left panel show the FOF member particles of halos comprising one, two and three major components in the cubic region $6 h^{-1} \text{ Mpc}$ a side around the halo. The FOF mass M_{FOF} of each halo is 8.43 , 7.88 and $3.18 \times 10^{14} h^{-1} M_{\odot}$, respectively. The ratios of mass of the second and third massive components (M_2 and M_3) compared to the mass of the most massive one (main halo) M_1 are also indicated in the three panels. The cumulative fractions of M_2/M_1 and M_3/M_1 for our 2004 FOF halos are illustrated in the lower-right panel. For example, $\sim 90\%$ of the halos have $M_2/M_1 < 0.2$. In this paper, we call the halos with $M_2/M_1 > 0.2$ “multiple-halos”. In this figure, the halos in the upper-right and lower-left panels are multiple-halos.

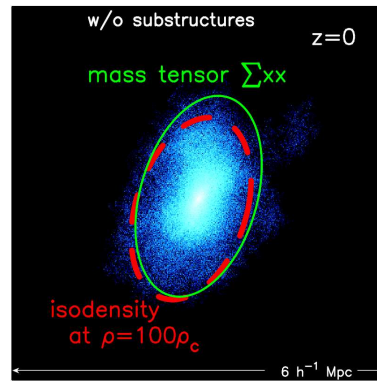


Fig. 2. Same as the top-left panel of Figure 1, but excluding substructures. The projection of the ellipsoid fitted to the isodensity surface at $\rho = 100\rho_c$ is shown in the red dashed curve. The ellipsoid enclosing the same mass as that inside the isodensity surface ($M_{\text{ellipsoid}} = 6.25 \times 10^{14} h^{-1} M_{\odot}$) is determined by using the mass tensor $I = \sum xx$ and its projection is plotted in the green solid curve. The resulting two ellipsoids are similar; $A_1/A_3 = 0.57$ (isodensity surface) and $A_1/A_3 = 0.55$ (mass tensor).

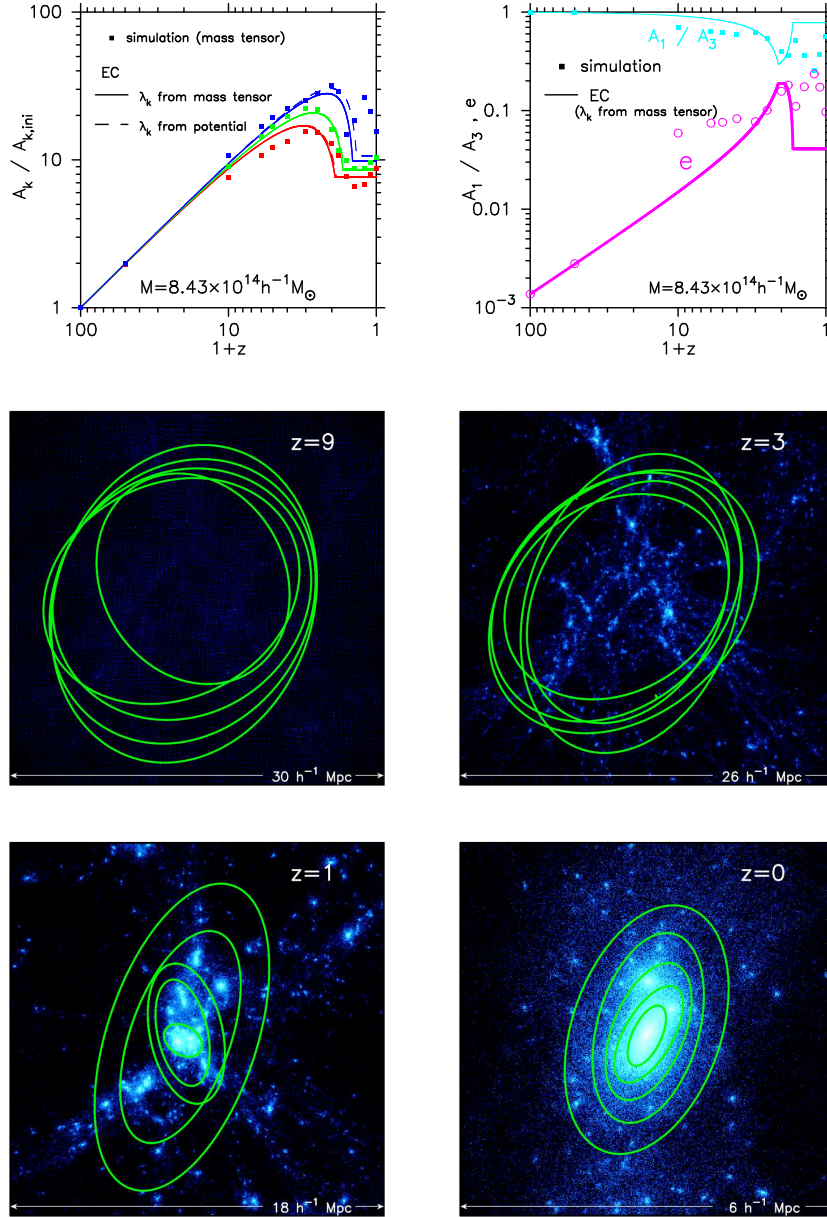


Fig. 3. Evolution of the single-halo ($M_{\text{FOF}} = 8.43 \times 10^{14} h^{-1} M_\odot$) plotted in the top-left panel of Figure 1. *top-left:* Evolution of the axis lengths A_k . The squares indicate A_k calculated from the mass tensor; A_1, A_2, A_3 are colored in red, green, blue, respectively. The solid lines indicate the EC prediction with the initial λ_k are calculated from A_k at $z = 99$ through Equation (7). The dashed lines are also the EC prediction, but the initial λ_k are eigenvalues of the tensor $\nabla_{ij} \phi / (4\pi G \bar{\rho} a^3)$ calculated from the top-hat smoothed density field at the scale $(3M_{\text{FOF}} / (4\pi \bar{\rho}))^{1/3}$. *top-right:* Evolution of the axis ratio A_1 / A_3 (cyan) and the ellipticity e (magenta); A_1 / A_3 : filled squares (simulation) and thin line (EC), e : open circles (simulation) and thick line (EC). *middle and bottom:* Density distributions around the halo at $z = 9, 3, 1$ and 0 . The projections of the ellipsoids are determined by the mass tensor $I = \sum xx$ for the five different mass scales inside the halos ($M = (s/5)M_{\text{FOF}}$; $s = 1, \dots, 5$) and plotted in green curves. All the particles including the non-FOF members are shown, and used in determining the ellipsoids.

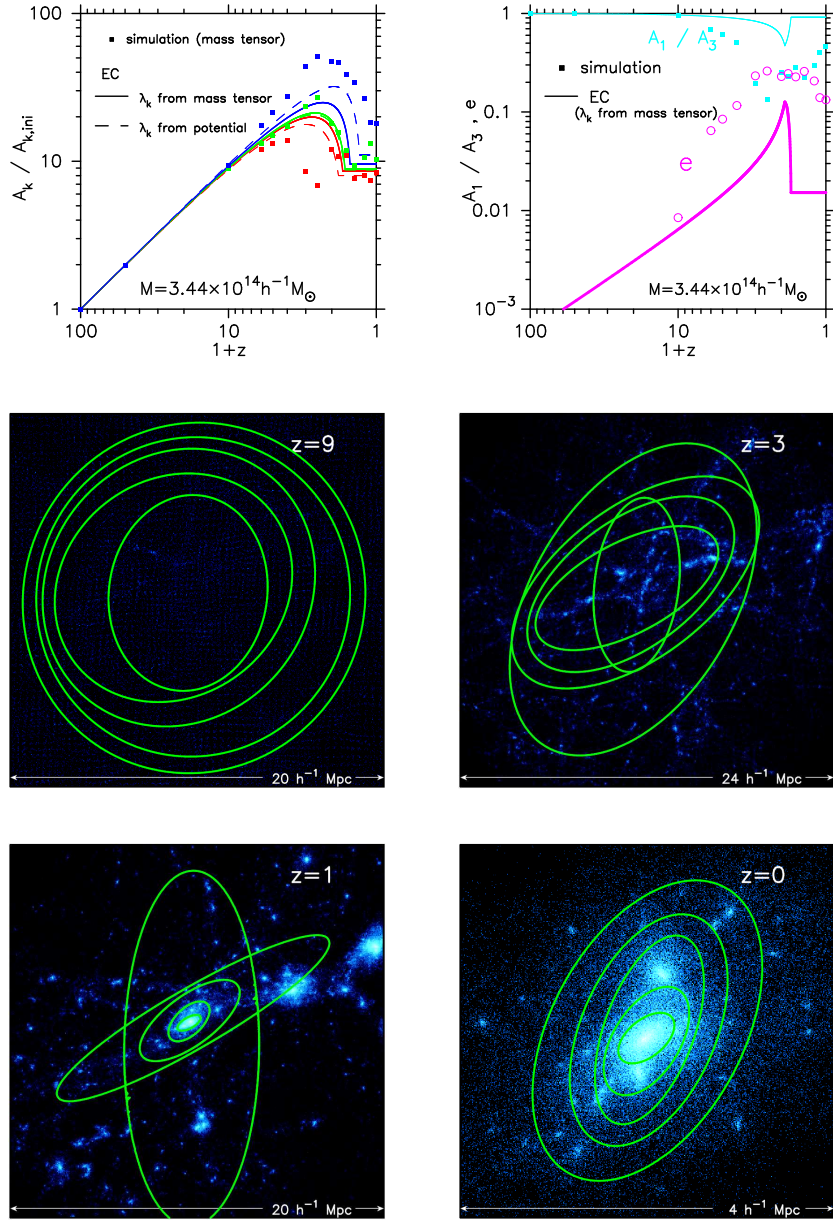


Fig. 4. Same as Figure 3, but for another single-halo ($M_{\text{FOF}} = 3.44 \times 10^{14} h^{-1} M_{\odot}$).

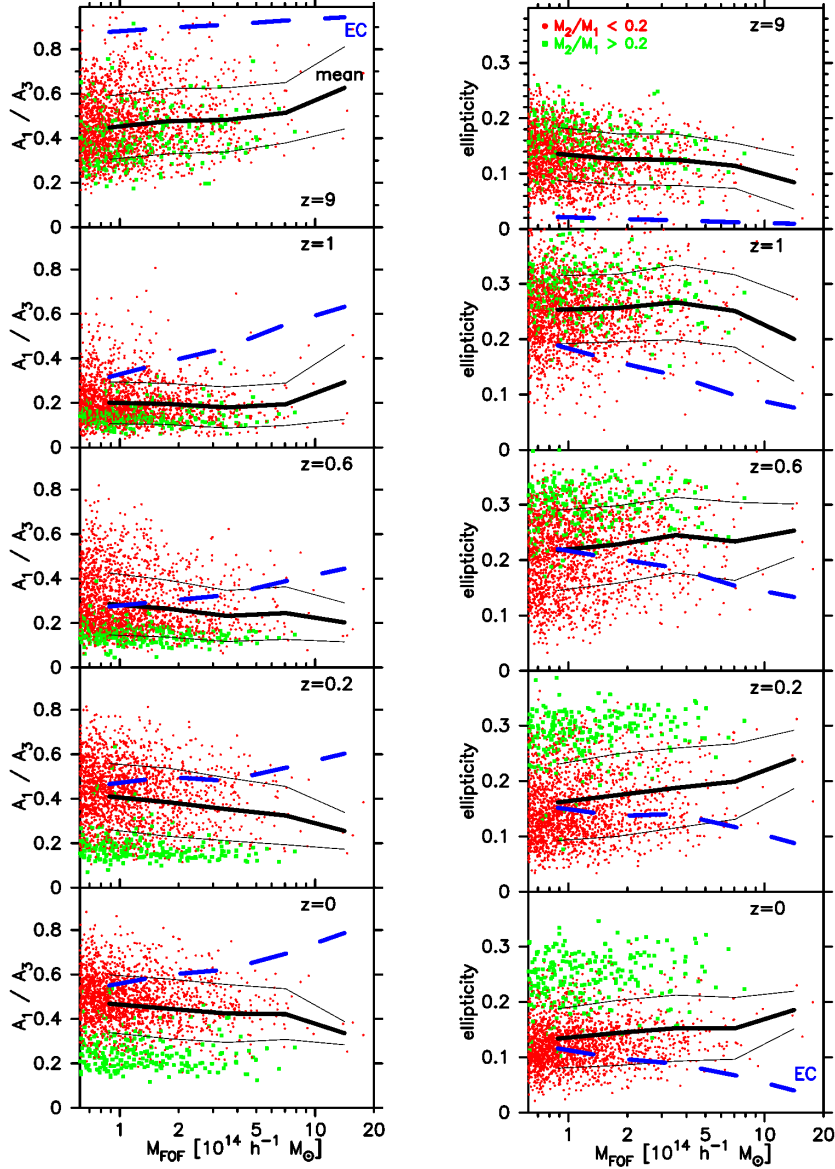


Fig. 5. Axis ratio A_1/A_3 (left) and ellipticity e (right) of each halo against its FOF mass M_{FOF} at the five different redshift ($z = 9, 1, 0.6, 0.2, 0$). Each symbol indicates the result for each of the 2004 simulated halos; red circle are single-halos ($M_2/M_1 < 0.2$), green squares are for multiple-halos ($M_2/M_1 > 0.2$). The thick and thin solid lines indicate the mean and the standard deviation, respectively, for all the halos. For comparison, the blue dashed line indicates the EC prediction, where the initial λ_k are the eigenvalues of the tensor $\nabla_{ij}\phi/(4\pi G\bar{\rho}a^3)$ calculated from the top-hat smoothed density field at the scale $(3M_{\text{FOF}}/(4\pi\bar{\rho}))^{1/3}$. Note that the multiplicity (M_2/M_1) of the halos is determined only at $z = 0$.

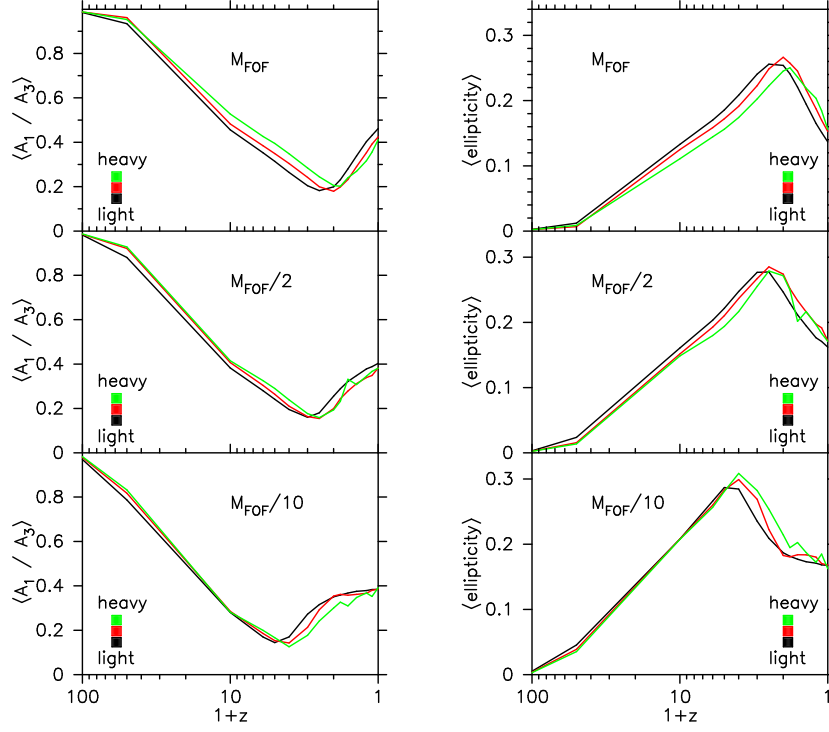


Fig. 6. Evolution of the axis ratio $\langle A_1/A_3 \rangle$ (left) and ellipticity $\langle e \rangle$ (right), averaged over the three different mass ranges ($M_{\text{FOF}} > 2.5 \times 10^{14} h^{-1} M_\odot$; green, $1.25 \times 10^{14} h^{-1} M_\odot < M_{\text{FOF}} < 2.5 \times 10^{14} h^{-1} M_\odot$; red and $6.25 \times 10^{13} h^{-1} M_\odot < M_{\text{FOF}} < 1.25 \times 10^{14} h^{-1} M_\odot$; black) at the three different mass scales (M_{FOF} ; top, $M_{\text{FOF}}/2$; middle, $M_{\text{FOF}}/10$; bottom).

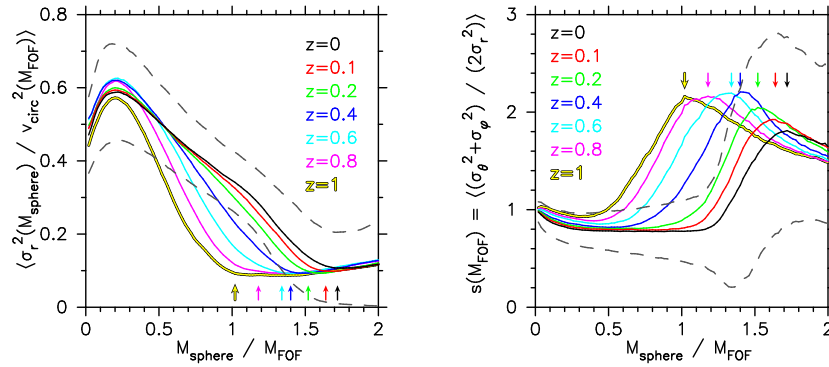


Fig. 7. Radial profiles of the radial velocity dispersion σ_r^2 (left) and the velocity isotropy measure $s = (\sigma_\theta^2 + \sigma_\phi^2) / (2\sigma_r^2)$ (right), averaged over the 2004 simulated halos, at the seven different redshifts; $z = 1, 0.8, 0.6, 0.4, 0.2, 0.1, 0$. The velocity dispersion in the left panel is normalized by the circular velocity $v_{\text{circ}}^2(M_{\text{FOF}}) = GM_{\text{FOF}}/R_{\text{FOF}}$ of each halo at each redshift. The dashed lines indicate the standard deviation for $z = 0$. At each redshift, the mass scale where s reaches a maximum is indicated by an arrow in both panels.

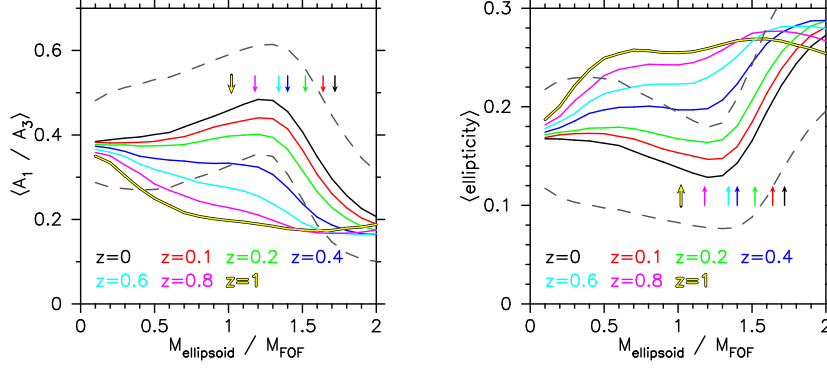


Fig. 8. Radial profiles of the axis ratio $\langle A_1/A_3 \rangle$ (left) and the ellipticity $\langle e \rangle$ (right), averaged over the 2004 simulated halos, at the seven different redshifts; $z = 1, 0.8, 0.6, 0.4, 0.2, 0.1, 0$. The dashed lines indicate the standard deviation for $z = 0$. At each redshift, the *spherical* mass scale where s reaches a maximum (Figure 7) is indicated by an arrow for both panels.

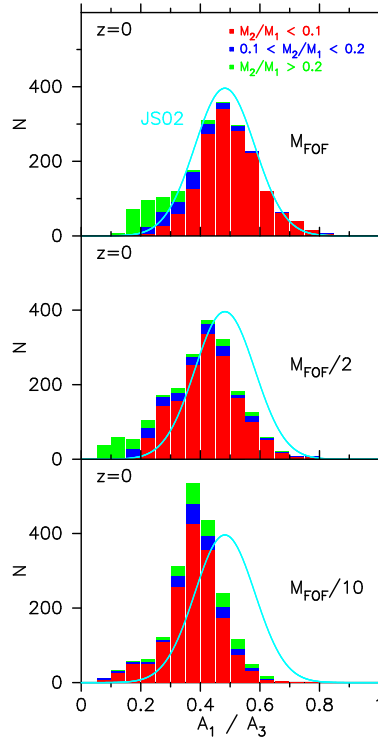


Fig. 9. PDF of the minor-to-major axis ratio A_1/A_3 of triaxial ellipsoid at $z = 0$ for the three different mass scales: $M_{\text{ellipsoid}} = M_{\text{FOF}}, M_{\text{FOF}}/2$ and $M_{\text{FOF}}/10$. The histogram is divided by three types of halos; $M_2/M_1 < 0.1$ (red), $0.1 < M_2/M_1 < 0.2$ (blue), $M_2/M_1 > 0.2$ (green). The cyan curve shows the fitting formula of JS02 (Equation (13)) that is based on the isodensity surface $\rho = 2500\rho_c$, approximately corresponding to $0.3r_{\text{vir}}$ and $M_{\text{FOF}}/10$.

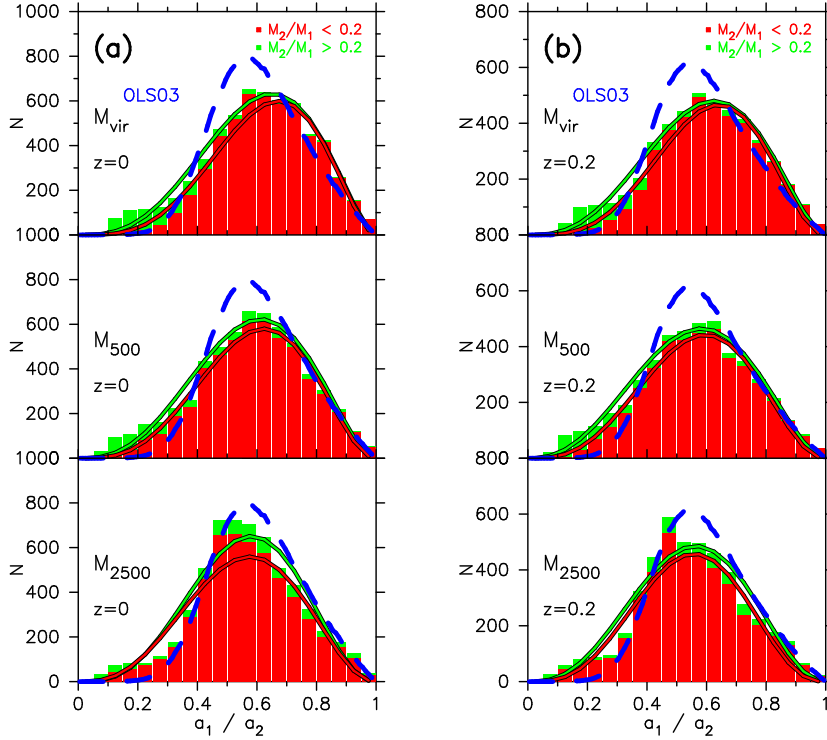


Fig. 10. PDF of the projected axis ratio at the three different mass scale M_{vir} , M_{500} and M_{2500} , for four redshifts; $z = 0$ (a), 0.2 (b), 0.4 (c), 1 (d). The solid curves show the best-fit beta distributions (our model). For comparison, the PDF by OLS03 (based on JS02) is also shown. The histogram is colored according to the multiplicity of halos; $M_2/M_1 < 0.2$ (red), $M_2/M_1 > 0.2$ (green). The multiplicity of halos (M_2/M_1) is determined separately at each redshift. When calculating the PDF of OLS03, $M = 2 \times 10^{14} h^{-1} M_{\odot}$, corresponding to the mean mass of our halos, is substituted in Equation (13). Only the simulated halos with $M_{\text{vir}}(z) > 6.25 \times 10^{13} h^{-1} M_{\odot}$ are selected at each redshift, and the number of halos is 3×2004 ($z = 0$), 3×1550 ($z = 0.4$), 3×1101 ($z = 0.2$), 3×317 ($z = 1$).

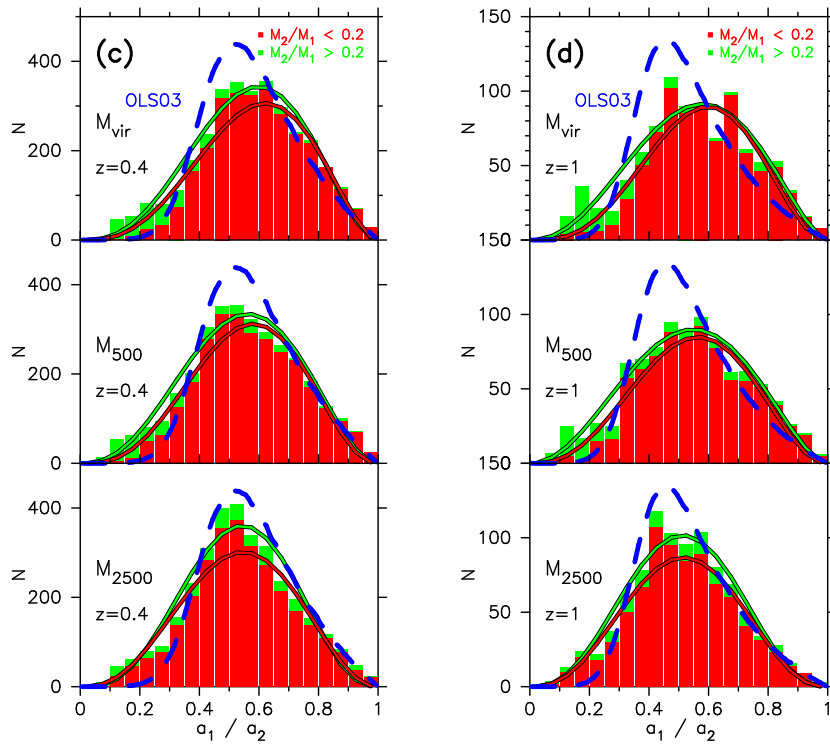


Fig. 10. Continued.

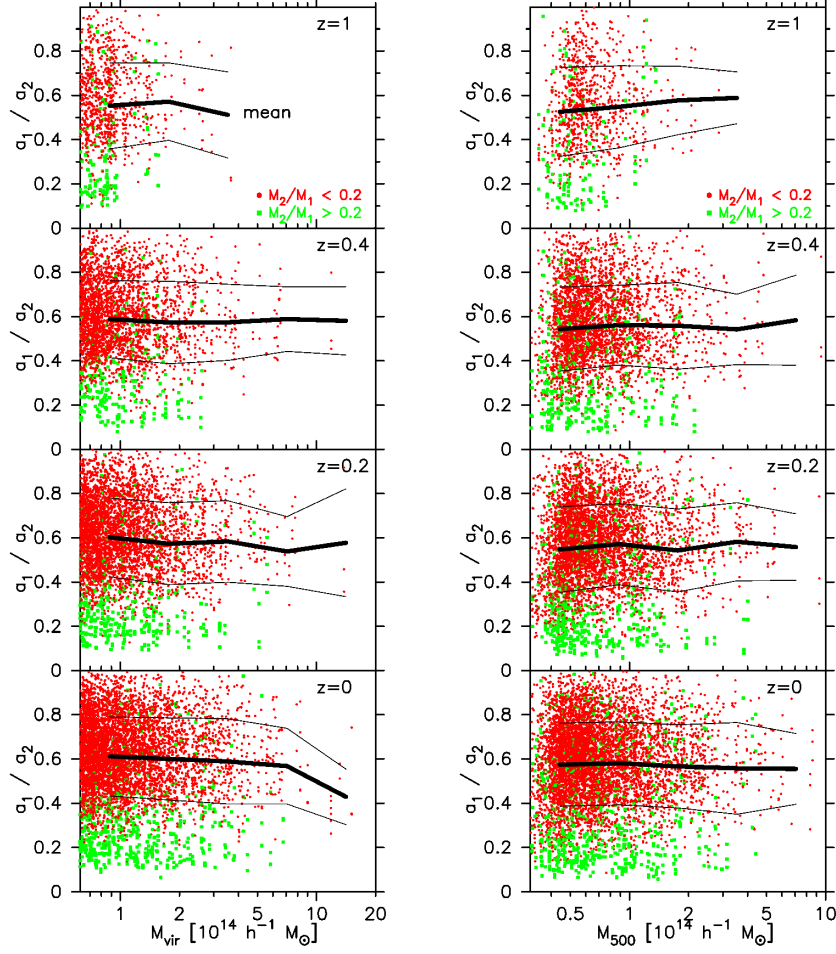


Fig. 11. Projected axis ratio a_1/a_2 of each halo at the four different redshifts ($z = 1, 0.4, 0.2, 0$) against its M_{vir} (left) and M_{500} (right). Each symbol indicates the result for each of the 2004 simulated halos; red circle are single-halos ($M_2/M_1 < 0.2$), green squares are for multiple-halos ($M_2/M_1 > 0.2$). The thick and thin solid lines indicate the mean and the standard deviation, respectively. The halos are identified at each redshift, and their multiplicity (M_2/M_1) is also defined at each redshift. The number of the simulated halos is 3×2004 ($z = 0$), 3×1550 ($z = 0.4$), 3×1101 ($z = 0.2$), 3×317 ($z = 1$).

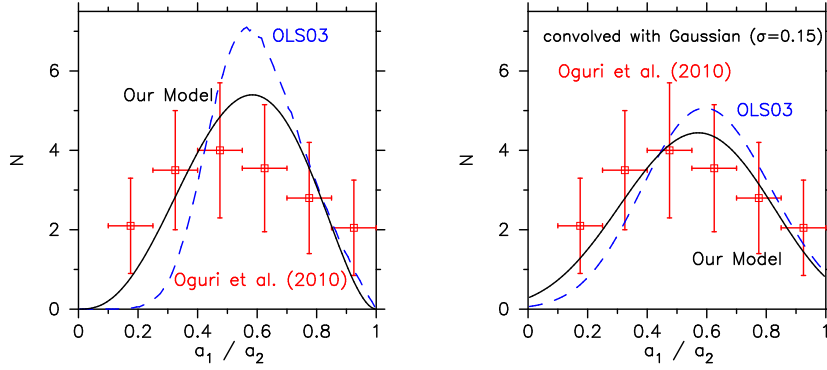


Fig. 12. Comparison of PDFs of projected axis ratio a_1/a_2 . The red symbols with error bars show the results from the 18 clusters in the weak lensing analysis by Oguri et al. (2010). The PDF of OLS03 is plotted in the blue dashed curve. Following Oguri et al. (2010), we use $M_{\text{vir}} = 7 \times 10^{14} h^{-1} M_{\odot}$, corresponding to the mean mass of the observed clusters, when calculating the PDF of OLS03 through Equation (13). The black solid curve indicate our fitting formula for the PDF of a_1/a_2 at M_{500} of all the halos at $z = 0.2$ (Table 2). For the PDF of OLS03 and ours, the left panel illustrates the original PDFs, while the right panel shows those convolved with the Gaussian function with $\sigma = 0.15$, corresponding to the typical uncertainty for a_1/a_2 in the lensing analysis (cf. Figure 3 and Table 1 of Oguri et al. (2010)).